



THE UNIVERSITY *of* EDINBURGH

Edinburgh Research Explorer

Catastrophic failure: how and when? Insights from 4D in-situ x-ray micro-tomography

Citation for published version:

Cartwright-taylor, A, Main, IG, Butler, IB, Fousseis, F, Flynn, M & King, A 2020, 'Catastrophic failure: how and when? Insights from 4D in-situ x-ray micro-tomography', *Journal of Geophysical Research. Solid Earth*, vol. 125, no. 8, e2020JB019642. <https://doi.org/10.1029/2020JB019642>

Digital Object Identifier (DOI):

[10.1029/2020JB019642](https://doi.org/10.1029/2020JB019642)

Link:

[Link to publication record in Edinburgh Research Explorer](#)

Document Version:

Peer reviewed version

Published In:

Journal of Geophysical Research. Solid Earth

Publisher Rights Statement:

©2020 American Geophysical Union. All rights reserved.

General rights

Copyright for the publications made accessible via the Edinburgh Research Explorer is retained by the author(s) and / or other copyright owners and it is a condition of accessing these publications that users recognise and abide by the legal requirements associated with these rights.

Take down policy

The University of Edinburgh has made every reasonable effort to ensure that Edinburgh Research Explorer content complies with UK legislation. If you believe that the public display of this file breaches copyright please contact openaccess@ed.ac.uk providing details, and we will remove access to the work immediately and investigate your claim.





Cartwright-Taylor Alexis (Orcid ID: 0000-0001-7805-4576)

Fusseis Florian (Orcid ID: 0000-0002-3104-8109)

Catastrophic failure: how and when? Insights from 4D in-situ x-ray microtomography

Alexis Cartwright-Taylor¹, Ian G. Main¹, Ian B. Butler¹, Florian Fusseis¹, Michael Flynn¹ and Andrew King²

¹School of Geosciences, University of Edinburgh, James Hutton Road, Edinburgh EH9 3FE, UK. ²SOLEIL Synchrotron, L'Orme des Merisiers Saint Aubin, Gif-sur-Yvette, France.

Corresponding author: Alexis Cartwright-Taylor alexis.cartwright-taylor@ed.ac.uk

Key Points:

- Micron-scale crack network evolution and localization is imaged *in-situ* in deforming granite samples with controlled initial heterogeneity
- Heterogeneity affects order and predictability of the phase transition to failure, which occurs as correlation length approaches grain size
- Correlation dimension of the crack population is a key indicator of localization, and anisotropy in starting porosity dictates fault strike

This article has been accepted for publication and undergone full peer review but has not been through the copyediting, typesetting, pagination and proofreading process which may lead to differences between this version and the Version of Record. Please cite this article as doi: 10.1029/2020JB019642

Abstract

Catastrophic failure of brittle rocks is important in managing risk associated with system-sized material failure. Such failure is caused by nucleation, growth and coalescence of micro-cracks that spontaneously self-organize along localized damage zones under compressive stress. Here we present x-ray micro-tomography observations that elucidate the *in-situ* micron-scale processes, obtained from novel tri-axial compression experiments conducted in a synchrotron. We examine the effect of microstructural heterogeneity in the starting material (Ailsa Craig micro-granite; known for being virtually crack-free) on crack network evolution and localization. To control for heterogeneity, we introduced a random nano-scale crack network into one sample by thermal stressing, leaving a second sample as-received. By assessing the time-dependent statistics of crack size and spatial distribution, we test the hypothesis that the degree of starting heterogeneity influences the order and predictability of the phase transition between intact and failed states. We show that this is indeed the case at the system scale. The initially more heterogeneous (heat-treated) sample showed clear evidence for a second-order transition: inverse power-law acceleration in correlation length with a well-defined singularity near failure, and distinct changes in the scaling exponents. The more homogeneous (untreated) sample showed evidence for a first-order transition: exponential increase in correlation length associated with distributed damage and unstable crack nucleation ahead of abrupt failure. In both cases, anisotropy in the initial porosity dictated the fault orientation, and system-sized failure occurred when the correlation length approached the grain size. These results have significant implications for the predictability of catastrophic failure in different materials.

Plain Language Summary

When rocks deform, tiny cracks appear, increasing in size and number until the rock breaks completely, often along a narrow plane of weakness where cracks have spontaneously aligned. Sometimes, when the microstructure is complicated, cracking accelerates quickly in a predictable way, giving a good indication of when the rock will break. In other cases, when the microstructure is more uniform, cracking accelerates more slowly and the rock breaks suddenly and early. To understand why failure is predictable in some cases but not others – a major problem in managing risk from material failure (e.g., earthquakes) – we used x-ray imaging to see how cracks form and interact with each other inside deforming rocks. We found that predictable behavior only arose when cracks aligned themselves asymmetrically. The orientation of this damage zone was governed by the rock's pre-existing microstructure. We also found distinct changes in crack size and spatial arrangement during alignment, indicating that the rock was approaching failure. However, when cracks did not align asymmetrically, similar changes were not observed and failure was not predictable. Our results are important because they help explain why reliable indicators of catastrophic failure are not always observed and why forecasting may only work in certain cases.

List of Symbols (in order of appearance)

variable	symbol
correlation length (typical linear dimension of largest void)	ξ
time	t
critical (failure) time	t_c
axial sample strain	ϵ
critical (failure) strain	ϵ_c
strain rate	$\dot{\epsilon}$
differential stress	σ
axial stress	σ_1
confining pressure (radially-symmetric)	σ_3
sample length	L
critical (failure) stress	σ_c
sample co-ordinate system	x, y, z
dip	ϕ
strike	θ
porosity	φ
number of segmented voids	N
individual void	i
volume of an individual void (pore or micro-crack)	V_i
volume of the largest void	V_{max}
sample radius	R
length of analyzed sub-volume	l
volume of analyzed sub-volume	V_{subvol}
corrected Akaike Information Criterion	AIC_c
first-order moment of inertia (void centroid)	M
second-order moment of inertia (covariance matrix)	I
void ellipsoid radius	r
mean void ellipsoid radius	\bar{r}
power-law exponent of void volume distribution	β
Euclidean distance between two voids (inter-void distance)	L_i
two-point correlation (fractal) dimension (power-law exponent of inter-void distance distribution)	D
cumulative complementary (survivor) function of frequency-volume distribution	$\Phi(V)$
completeness threshold of frequency-volume distribution	V_t
tapering corner threshold of frequency-volume distribution	V_c
modified Bayesian Information Criterion	BIC
incremental probability distribution of inter-void lengths	$P(L_i)$
exponent of incremental inter-void length distribution	D_{inc}

1 Introduction

Catastrophic failure of rocks in the brittle Earth is a critically-important driving mechanism for phenomena such as landslides, volcanic eruptions and earthquakes, including induced seismicity. Such failure often happens suddenly and with devastating consequences, occurring when structural damage, in the form of smaller faults and fractures, concentrates within localized zones. Damage localization leads to weakening and stress redistribution, eventually resulting in system-sized brittle failure along a distinct and emergent fault plane. Localized damage is pervasive at all scales throughout the brittle crust (Mitchell and Faulkner, 2012) and is therefore a fundamental control on catastrophic failure. Crack nucleation and growth, and crack coalescence within already localized zones, are relatively well-understood from microstructural and field observations of damaged rocks, and from monitoring and locating earthquakes and acoustic emissions (elastic wave packets released during laboratory-scale micro-fracturing events). However, the process of localization remains elusive. Smaller cracks spontaneously self-organize along the incipient fault plane, often immediately before failure, but the precise mechanisms involved in this self-organization have yet to be determined. Open questions include: (i) how do cracks, pores and grain boundaries interact locally with the applied stress field to cause catastrophic failure to occur at a specific place, orientation and time? (ii) why can we detect precursors to catastrophic failure only in some cases?

Fractures and faults have a self-similar structure; they are scale-invariant in their length and spatial distributions (Main et al., 1990; Main, 1996; Bonnet et al., 2001), and in the way their size relates to the energy released during rupture (Abercrombie, 1995; Goodfellow and Young, 2014). Remarkably, earthquakes and acoustic emissions (AE) are indistinguishable apart from the absolute source size, with scaling characteristics that are invariant over 15 orders of magnitude (Goodfellow and Young, 2014). This behavior is controlled by the local stress state and rock mass properties. Classically, brittle rock deformation and failure have been characterized by AE, with progressive cracking in heterogeneous materials under stress leading to systematic changes in the AE event rate and its frequency-magnitude distribution. Experiments have shown that pervasive microcracking accumulates in the sample sub-critically, i.e., without causing system-sized failure (Lockner et al., 1991; Lei et al., 2000), until the accumulating cracks self-organize along an asymmetric, localized damage zone. System-scale failure then occurs when nucleating micro-cracks have localized sufficiently for a runaway positive feedback of self-sustaining crack propagation and coalescence to take over (Main et al., 1993). In some cases, this self-organization becomes evident in the emergence of an inverse power-law acceleration of event rate with a well-defined failure time. In others, system-sized failure of rock samples is commonly associated with the transition from an exponential increase to a sudden, rapid acceleration in the AE event rate close to peak stress (Sammonds et al., 1992; Moura et al., 2005; Vasseur et al., 2015). This transition occurs exactly when cracks begin to localize along the incipient fault plane (Lockner et al., 1991). At this crucial point, nucleated cracks grow by jumping geometrical and rheological barriers, so regions of stress concentration must already be correlated at the scale of the incipient fault network (Sammis and Sornette, 2002). The organized fracture network then propagates dynamically, with macroscopic failure occurring at a well-defined, finite time as the power-law reaches its asymptote.

This behavior indicates a transition from pervasive but stable crack growth, controlled by the sample's microstructure, to an unstable regime of dynamic rupture along an organized fracture network, controlled by stress and fracture mechanics (Guéguen and Schubnel, 2003; Alava et al., 2008). The inverse power law transition can be described as a critical or second-order phase transition; a continuous transition from one state to another, during which the

system becomes extremely susceptible to external factors. It is second-order if the first derivative of the free energy of the system (an entropy term) changes continuously as a function of the control parameter, e.g., temperature (Stanley, 1971, Fig. 2.6) or, in the case of a constant strain (or stress) rate rock deformation experiment, strain (or stress). This is associated with an inverse power law acceleration of the correlation length towards the critical point (Bruce and Wallace, 1989). At this point, strong correlations exist between all parts of the system (including at long-range) and many length scales become relevant (resulting in a self-similar structure and power-law scaling), with events occurring at all relevant length scales (associated with broadband self-similarity of correlations). The transition to an inverse power-law in the AE event rate, with its ‘finite-time singularity’ at failure, is also characteristic of a second-order or critical phase transition (Sammis and Sornette, 2002). If this occurs in the lead up to macroscopic failure, then the failure time can be forecast accurately (Vasseur et al., 2015; 2017). Inverse power-law acceleration to a well-defined failure time has also been seen in the evolving microstructure (micro-crack porosity and the volume of the largest micro-fracture) of crystalline rocks undergoing brittle deformation (Renard et al., 2017; 2018).

However, the evolution of damage does not always allow a fit to a model with a well-defined failure time. In structurally homogeneous materials, there is no emergent, smooth power-law acceleration to failure, as shown experimentally by Vasseur et al. (2015; 2017) for a range of rock types and material analogues. In the extreme case of a single flaw in an otherwise uniform starting material, there is no precursor, and catastrophic system-sized failure occurs suddenly when the flaw propagates dynamically at a maximum in the system free energy. In turn, this depends on the applied stress, the length of the starting flaw, and the specific surface energy of the material (Griffith, 1921; 1924). This results in a discontinuous or first-order transition between intact and failed states. In real materials that possess only a small amount of microstructural disorder, progressive subcritical cracking, i.e., cracking which does not fulfil the conditions for sustained propagation, shows only an exponential increase in the event rate time-to-failure behavior (Vasseur et al., 2015; 2017). Failure occurs suddenly and early; often much earlier than expected from an exponential asymptote (Vasseur et al., 2015; 2017). This behavior is also characteristic of an abrupt first-order transition, with the exponential behavior reflecting local correlations (Stanley, 1971; Sethna, 2006).

Phase transitions are often characterized by the evolution of the correlation length and scaling exponents of the system in question (Stanley, 1971). The correlation length, ξ , is the distance over which the effects of a local perturbation of the system will spread (Thouless, 1989). Close to a critical point, the system can be viewed as made up of regions of size ξ in the critical state. In this case, ξ can be interpreted as the size of the regions of the nucleating phase, or the typical linear dimension of the largest piece of correlated spatial structure (Bruce and Wallace, 1989), which in our case is approximately the length of the largest fracture. As the two phases (intact and failed) compete to select the final equilibrium state, regions closer than ξ are correlated and those further apart are uncorrelated. Approaching the critical point, the correlated (nucleating) regions become comparable to the system size. Thus, the maximum correlation length, and associated parameters such as the maximum AE magnitude, are restricted by the system size.

During a first-order transition, the correlation length ξ becomes macroscopically large but remains finite until the discontinuity at the sudden change of state (Stanley, 1971). In the case of a single Griffith crack, the correlation length is simply the length of the starting flaw, which suddenly becomes system-sized at failure as the flaw propagates instantaneously through the material (Figure 1, blue line). When real, structurally homogeneous materials, with a dilute population of material flaws, undergo progressive subcritical cracking (e.g., Vasseur et al., 2015; 2017), we expect the correlation length to increase exponentially but remain finite until

it becomes system-sized at a sudden-onset discontinuity (Figure 1, orange line). Conversely, during a continuous phase transition, the correlation length ξ becomes effectively infinite (Figure 1, green line), growing as an inverse power-law function of the control parameter (e.g., temperature), T , approaching the critical point, T_c (Bruce and Wallace, 1989):

$$\xi \sim (T_c - T)^{-\nu} \quad (1)$$

This is the type of behavior is associated with progressively more heterogeneous materials undergoing brittle deformation (Vasseur et al., 2015; 2017). In summary, the degree of microstructural disorder of a material exerts a strong control on the type of phase transition from subcritical crack growth to dynamic rupture, and consequently the predictability of the transition. In particular, experiments (Vasseur et al., 2017) and models (Kun et al., 2018) have shown that heterogeneity strongly influences the spatial distribution of micro-cracks at failure.

Here we investigate the impact of material heterogeneity on the nature of the phase transition between intact and failed states, and the associated predictability of failure, at the micron-scale. We show how the micro-crack network evolves within a deforming crystalline rock with different amounts of disorder. Since pre-existing cracks are the most dominant factor of all heterogeneities that govern the fault nucleation process in laboratory rock samples (Lei et al., 2000), we deformed two samples of Ailsa Craig micro-granite: one being an as-received control (nominally crack-free), and the other containing a pre-existing nano-scale crack network, induced by thermal stress, as a proxy for increased heterogeneity. Ailsa Craig samples, as received from the quarry, have no detectable cracks on thin sections under both optical and scanning electron microscopes (Meredith et al., 2005; 2012). They are an extreme end member of lowest crack density in natural rocks. Through the analysis of 4D, *in-situ* synchrotron x-ray micro-tomography (μ CT) images of the two samples undergoing tri-axial deformation (see Cartwright-Taylor et al. (2020) for access to the dataset), we test the hypothesis that the transition to failure is abrupt and unpredictable (first-order) in the as-received sample (our initially crack-free end member), but is continuous and predictable (second-order) in the pre-cracked sample. *In-situ* observation of the deforming microstructure allows us to measure directly the relevant parameters such as the correlation length and the scaling exponents.

We find that increasing the microstructural disorder affects the geometry, size and spatial distribution of the evolving micro-fractures. Using a combination of visual inspection of the μ CT images, geometrical analysis of the evolving crack network, and techniques used in statistical seismology, we show that the micro-crack network evolution varies significantly between the two samples. The degree of starting heterogeneity controls (i) the evolving spatial clustering and anisotropy of the micro-cracks, and (ii) the order of the phase transition. The initially crack-free sample exhibits an exponential increase in damage that reflects local correlations, a finite correlation length, and no obvious precursors to failure. In contrast, the pre-cracked sample exhibits emergent power-law behavior, an inverse power-law acceleration to infinite correlation length and clear precursors to failure. However, though the parameters may be different, the power-law scaling of the micro-crack volume and inter-crack length distributions, and some crack growth characteristics, appear independent of heterogeneity. Allowing for the fact that such microscopic failure characteristics may not be detectable above ambient noise in a field experiment, this may explain why measureable geophysical precursors to catastrophic failure events are detected only in some cases.

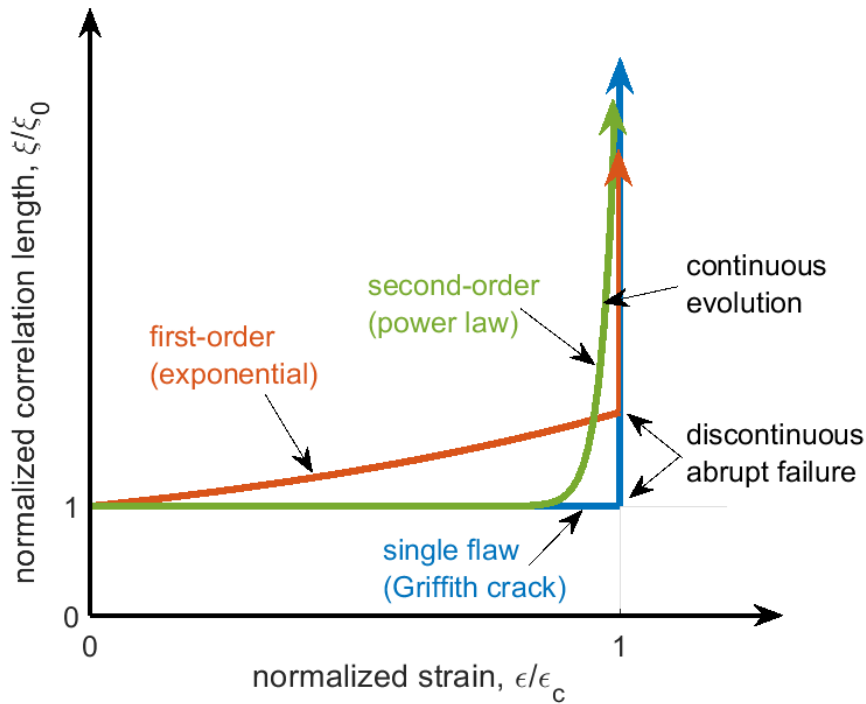


Figure 1: Schematic graph showing the expected behavior of the correlation length ξ , normalized by its initial value ξ_0 , as strain ϵ increases towards failure at critical strain ϵ_c for the three phase transition cases described in the text. The Griffith crack (blue line) and the exponential (orange line) are both examples of first-order transitions, exhibiting abrupt failure evident as the discontinuity in ξ at ϵ_c . The inverse power-law (green line) shows the smooth, continuous evolution to failure characteristic of a second-order transition.

2 Materials and Methods

2.1 Ailsa Craig micro-granite and thermal stressing

We used Ailsa Craig micro-granite (ACM) from the island of Ailsa Craig in the Firth of Clyde, Scotland. ACM is an extremely rare type of silica-unsaturated, alkali-rich microgranite, known as Blue Hone (Meredith et al., 2012). As received from the quarry, no pre-existing microcracks are detectable either by optical or scanning electron microscopy (Meredith et al., 2005; 2012). Porphyritic in texture with a groundmass of mean grain size 250 μm , ACM contains sparsely distributed microphenocrysts (up to 1.5 mm) of alkali feldspar (Odling et al., 2007). Clint et al. (2001) found it to have extremely low porosity ($\ll 1\%$) and permeability ($1.5 \times 10^{-23} \text{ m}^2$ at 10 MPa effective pressure), indicating that the small amount of pre-existing pores are predominantly unconnected (e.g., see Fig. 3 top left in Meredith et al., 2012). These properties make ACM ideal both for its main commercial use as the running surface of curling stones, and for the purposes of this study. We chose ACM for two main reasons: (i) its small grain size (250 μm) and (ii) its virtually crack-free nature. The former is essential to ensure a statistically significant number of grains (>10 grains per diameter) in the small (3 mm diameter x 9 mm long) cylindrical samples, and so to ensure that such small samples are representative of the rock as a whole. The latter is essential to allow comparison between two extreme end-members: (i) an as-received control sample with the lowest possible (to our knowledge) pre-existing crack density, and (ii) a second sample (from the same small block) containing a thermally-induced crack network imprinted over the nominally crack-free microstructure, thus increasing its heterogeneity compared with the initially crack-free (untreated) sample.

To introduce a network of micro-cracks, one sample was heated slowly to 600 $^{\circ}\text{C}$ prior to deformation. Thermal stressing is one of the key fracture-generating mechanisms in crustal rocks and is an effective method for introducing micro-fractures into rock samples. Heating ACM to elevated temperatures ($>500\text{ }^{\circ}\text{C}$) induces significant, permanent micro-crack damage, evident from photomicrographs (Meredith et al., 2012) and up to 50% and 30% reduction in P- and S- wave velocities respectively (Clint et al., 2001). Scanning electron micrograph observations (Odling et al., 2007) show that heating ACM to 900 $^{\circ}\text{C}$ causes the formation of a permanent micro-crack network with average aperture of 0.3 μm formed by tensile failure, with each crack nucleating halfway along a previous one to generate fracture intersections of primarily T-shaped geometry. The thermally-induced crack network is not discernible in our μCT data because this aperture is less than one tenth the length of one pixel (2.7 μm). Due to the partial volume effect, micro-cracks with an aperture smaller than half a pixel are not visible (e.g., Voorn et al., 2013).

2.2 Experimental apparatus, sample assembly and loading protocol

Synchrotron x-ray microtomography (μCT), in combination with x-ray transparent pressure vessels (e.g., Fusses et al., 2014; Renard et al., 2016; Butler et al., 2017), allow the microstructural evolution of deforming rock samples to be imaged directly, non-invasively and *in-situ* during an experiment. This provides a critical advantage over conventional deformation experiments, where the evolution of microscopic deformation cannot be inferred from post-test analysis of the microstructure because it is heavily overprinted by extensive damage caused during the macroscopic rupture process. Even in the case where conventional experiments are stopped immediately prior to macroscopic failure, overprinting occurs when the hydrostatic and differential stresses are released during extraction of the sample from the steel-walled pressure vessel, resulting in permanent damage and hysteresis. *In-situ* x-ray μCT imaging overcomes both these issues, as well as providing detailed microstructural information about

the temporal evolution of damage accumulation at a much higher temporal resolution. A single time-resolved experiment is equivalent to tens of conventional experiments with *ex-situ*, post-experiment analysis, and has the virtue that the same sample is observed at each time-step rather than a suite of samples, removing the issue of sample variability.

In our experiments, each sample of ACM underwent tri-axial deformation to failure. The experiments were conducted using a novel, miniature, lightweight (<1.3 kg) x-ray transparent tri-axial deformation apparatus Mjölfnir', developed and tested at the University of Edinburgh. Mjölfnir, named for the hammer of Thor, the Norse god of thunder, accommodates samples of 3 mm diameter and up to 10 mm in length and is designed to operate up to confining pressures of 50 MPa and axial stress in excess of 622 MPa (Butler et al., 2017). For this study, Mjölfnir was installed on the μ CT rotation stage at the PSICHE beamline at SOLEIL Synchrotron, Gif-sur-Yvette, France (Figure 2a,b). Two cylindrical samples of ACM, one heat-treated and one untreated were cored using a diamond core drill and the ends ground flat and parallel to achieve 3 mm outside diameter and 9 mm length, compared to the typical grain size of 250 μ m. Even though this sample diameter is very small (required to obtain high-resolution μ CT images), the small grain size means that there are more than 10 grains per diameter, ensuring that such small samples are representative of the rock as a whole. The sample was assembled between the two pistons, jacketed with silicone tubing (3.18 mm internal diameter and 0.79 mm wall thickness), and protected from the confining fluid using twisted wire loops to seal the jacket against the piston (Butler et al., 2017). The pressure vessel was lowered over the sample assembly and fixed into place. A confining pressure of 15 MPa was then applied and maintained during the test. A hydrostatic starting pressure condition was achieved by simultaneously increasing the axial pressure to match the confining pressure. Delivery of the pressurizing fluid, deionized water, to the hydraulic actuator and pressure vessel was achieved using two Cetoni neMESYSTM high pressure syringe pumps operated with QmixElementsTM software.

Experiments were conducted at room temperature under nominally dry conditions. A reference μ CT scan was acquired at zero differential stress to obtain the initial state of the sample prior to loading. The sample was then loaded to failure at a constant strain rate of $3 \times 10^{-5} \text{ s}^{-1}$ in a step-wise manner, with steps of 20 MPa to start with, decreasing to 10 MPa from 70% of the failure strength and then 5 MPa once the sample started to yield (Figure 2c). At each step the stress was maintained and a μ CT volume acquired. To accommodate the full sample length at maximum resolution, three sequential scans were acquired at different positions along the length of the sample and then stacked. For each position the corresponding projections that comprised the full length of the sample were tessellated and merged to create a single projection used for reconstruction of the whole sample in one μ CT volume. Each full set of scans was acquired in approx. 10 minutes. For each sample, 15 sets were acquired during loading with an additional set acquired after the main failure. For the heat-treated sample, this included one set at peak differential stress of 185 MPa. This μ CT volume contained the incipient fault at the critical point of failure, and the sample failed immediately upon continuation of the loading procedure. The untreated sample reached a peak stress of 182 MPa but failed before it could be scanned at this stress. The last pre-failure scan was at 177 MPa (97% of the critical failure stress, σ_c).

The differential stress is $\sigma = \sigma_1 - \sigma_3$, where σ_1 is the axial stress (the product of the measured ram pressure and the difference in area between the ram and the sample cross-section) and σ_3 is the radially-symmetric confining pressure. Axial sample strain was calculated as $\epsilon = \delta L/L_0$, where δL is the change in length of the sample between the starting μ CT volume and the volume of interest and L_0 is the initial length of the sample. It was obtained

directly from the reconstructed μ CT volumes by measuring the length change of the rock core between two fixed locations in each volume.

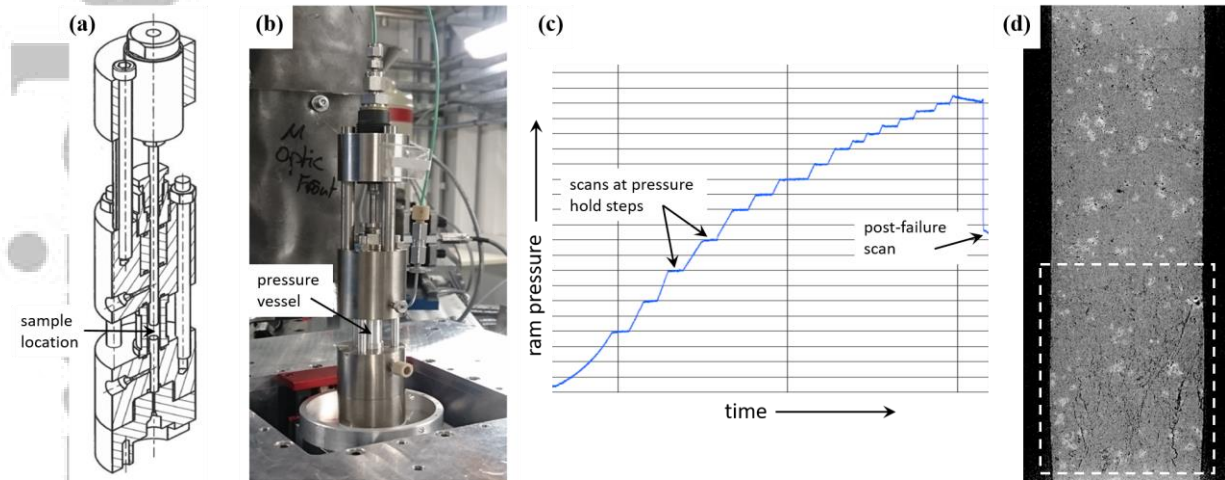


Figure 2: Our x-ray transparent deformation apparatus, Mjölfnir, in (a) schematic (Butler et al., 2017), and (b) installed at the PSICHE beamline. (c) Stepped loading procedure. (d) Reconstructed μ CT image showing damage accumulation at one end of the sample (this occurred in both samples) – dashed white line shows the analyzed sub-volume.

2.3 X-ray imaging and image data pre-processing

X-ray μ CT data was acquired using an sCMOS (scientific Complementary-Metal-Oxide Semiconductor) Hamamatsu ORCA Flash4.0 camera, with a Rodagon 50 lens, giving about 2.5x magnification (effective pixel size 2.7 μ m), and a 250 μ m thick LuAG:Ce scintillator. The white beam with an average detected energy of about 66 keV was filtered with 1 mm aluminium and 0.5 mm tungsten. During each scan, 1200 projections were acquired over 180°, with an exposure time per projection of 15-19 ms depending on the progressive darkening of the objective lens. A mix of absorption and phase contrast data was acquired, with a sample to detector distance of 125 mm.

Each μ CT volume was reconstructed by filtered back projection. Reconstructions were performed at the PSICHE beamline, using both x-ray absorption and phase contrast modes as implemented in the PyHST2 software (Mirone et al., 2014), and yielded 3D volumes of 1700 x 1700 x 4102 equidimensional voxels, with a voxel edge length of 2.7 μ m. These volumes were then processed to extract the fracture network from the reconstructed images. To deal efficiently with the huge size of each 3D volume (approx. 40 GB) and speed up the subsequent processing, we selected a sub-volume of interest – the region in the failed samples where the majority of damage had accumulated (Figure 2d, Table 1). Using the AvizoTM software package, this sub-volume was extracted from each of the full 3D volumes and de-noised with an anisotropic diffusion filter (stop value 0.4 over 4 iterations), which was chosen to emphasize the microcrack features as it preserves strong edges and enhances edge contrast. It was then down-sampled to 16-bit with a 32-bit threshold range of -0.3 to 0.8, yielding individual datasets of manageable size (approx. 3 GB).

Table 1: Dimensions of the whole sample and analyzed sub-volume, with uncertainties to two decimal places.

sample	sample diameter (mm)	sample length (mm)	ROI length (mm)	ROI area (mm ²)	ROI volume (mm ³)
untreated [ACfresh02]	2.96	8.73	3.33	6.62	22.03

2.4 Segmentation

Each dataset of 3D grey-scale images was then segmented to separate from the rest of the rock matrix the pre-existing pores and the evolving deformation-induced cracks in a binary fashion. Herein we use the term ‘porosity’ to include all the segmented void space in the sample, whether pre-existing (and therefore associated with the igneous history of the rock) or deformation-induced. We use the term ‘void’ to describe an individual segmented object.

Although easily distinguishable by the human eye, narrow planar features such as fractures are difficult to extract automatically from large 3D image datasets. This is due to the range of greyscale values accommodated by fractures of different apertures and the increasing similarity of these grey-values to the surrounding rock matrix as the aperture decreases. The main reason for this is the partial volume effect, whereby voxels containing both air and rock matrix appear brighter than voxels containing air alone. Fracture surface roughness and narrow apertures contribute to this effect. We used a multiscale Hessian fracture filter (MSHFF) technique to meet these challenges while still using an automated approach and segment the micro-cracks from the image data. This technique, developed and described in detail by Voorn et al. (2013), uses the Hessian matrix (second-order partial derivative of the input image data) to represent the local curvature of intensity variation around each voxel in a 3D volume (e.g., Descoteaux et al., 2005). Attributes of this local curvature can be used to distinguish planar features in the dataset (Text S1a in our Supporting Information, SI). The analysis is conducted over a range of observed crack apertures, which are combined to produce the final multiscale output: narrow fractures of varying apertures detected within the 3D image data. The analysis was carried out using the macros for FIJI (Schindelin et al., 2012) published by Voorn et al. (2013), utilizing the FeatureJ plugin (Meijering, 2010) to calculate the Hessian matrices, with input parameters given in (Table 2).

Table 2: Input parameters for segmentation code. Definitions given in Voorn et al. (2013).

smin	smax	sstep	blocksize	avgmat	consthresh	maxma t	paddin g	mincal	maxcal
2	8	1	1037	65535	0	56540	0	0.14118	0.32549

The binary segmented volumes were labelled and an intensity radius threshold of 15 to 100 applied followed by a small spot filter to remove round segmented objects with a radius of <50 pixels (134 μm) for visual clarity of the fault plane (Figure 3a). The local aperture at each voxel of the segmented voids was computed from the diameter of the largest ball containing the voxel and entirely inscribed within the object (Hildebrand and Ruesegger, 1997). Even with the segmentation method described, there is still significant under-sampling of the void population, particularly at the narrower end of the aperture range (Figure 3b). Further work in this area is required and would benefit from machine learning approaches (Andrew, 2018).

We present the data according to a co-ordinate system (x, y, z) where z is the vertical axis, which is parallel to the loading direction and corresponds to the direction of axial stress (σ_1). The other two (x and y) are the horizontal axes, which are perpendicular to the loading direction and correspond to the confining stress ($\sigma_2 = \sigma_3$) with their directions arbitrarily assigned but consistent between the two experiments. Void orientations are given in terms of their dip ϕ (deviation from horizontal) and strike θ (deviation from y).

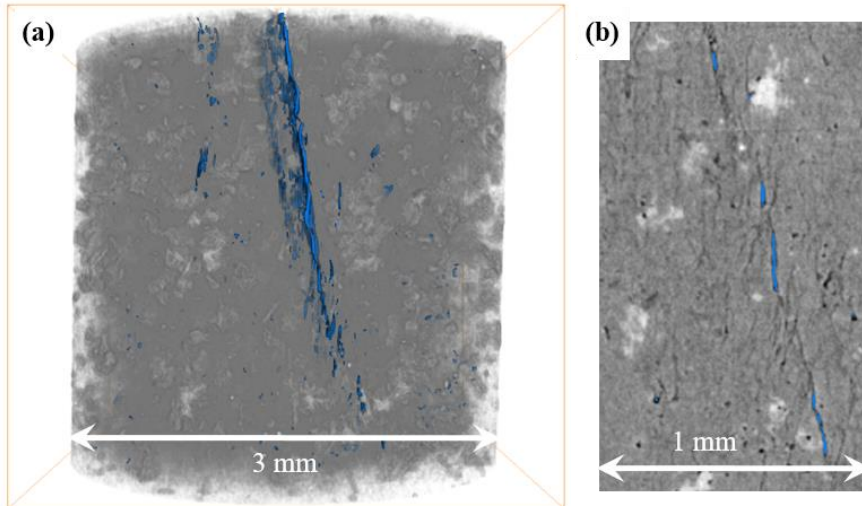


Figure 3: (a) Segmented fracture network (blue) within a greyscale 3D μ CT sub-volume at peak stress in the heat-treated sample. (b) Example of a 2D grey-scale slice, also with segmented fractures highlighted in blue. Most of the very narrow fractures remain undetected due to the similarity of the grey-scale values with the surrounding material.

2.5 Analysis of the segmented microcrack network

2.5.1 Porosity and the number of fractures

Initially of interest is the evolution of porosity, φ (including both the pre-existing pores and the developing micro-cracks) and the total number of voids, N , in each 3D sub-volume as deformation progressed. Due to the irregular shape of the segmented objects, and to take into account crack coalescence, one void was defined as all objects that were connected at least by the apex of a corner. To obtain N , each individual void, i , was assigned a label using the Label Analysis module in AvizoTM. Porosity was obtained from the total void volume divided by the analyzed sub-volume: $\varphi = (\sum V_i)/(\pi R^2 l)$, where V_i is volume of each crack, R is the sample radius and l is the length of the analyzed sub-volume. To determine the most likely empirical relationship with strain for both φ and N , we found the parameters for several possible models (quadratic, exponential and simple power-law) using non-linear least-squares regression and then used the corrected Akaike Information Criterion, $AICc$ (Hurvich and Tsai, 1989) to test these competing models objectively (see Text S2 in the SI for a full description of the calculations).

2.5.2 3D micro-crack orientations and geometries

These were obtained from the binary segmented data using an object-based approach to determine the best-fitting ellipsoid around each segmented void (pore or micro-crack). Each ellipsoid was calculated independently from the crack's 3D moments of inertia (Text S1b in SI), also using the Label Analysis module in AvizoTM. First-order moments, M , define the void's center of mass (centroid). Second-order moments, I , define the inertia (or covariance) matrix, with eigenvectors representing the ellipsoid axes orientations. Major, minor and medium ellipsoid radii, r , were computed as $r = \sqrt{5|\text{eigenvalue}|}$ from each corresponding eigenvalue of the inertia matrix (Ollion et al., 2013).

2.5.3 Crack network scaling exponents and correlation length

To find evidence for the type of phase transition undergone by each sample, we obtained the following indicators of critical point behavior: the correlation length, ξ (linear dimension of the largest void), the void size exponent, β , and the void separation exponent, or correlation dimension, D . These time-dependent parameters are equivalent to those commonly used to quantify the evolution of seismicity from acoustic monitoring (Aki, 1965; Sykes and Jaumé, 1990; Bufe and Varnes, 1993; Sornette and Sammis, 1995; Turcotte, 1997; Ouillon and Sornette, 2000; Zöller et al., 2001; Kagan, 2002; Sammis and Sornette, 2002; Tyupkin and Giovambattista, 2005). In rock deformation studies (e.g., Moura et al., 2005; Lei and Satoh, 2007), these parameters have been similarly inferred from the amplitudes and locations of acoustic emissions (AE). In particular, the inter-crack distance inferred from AE is a key parameter that controls the failure time and hence the accuracy of failure-time forecasts (Vasseur et al., 2017).

In this study, we obtained ξ , β and D directly from the evolving population of micro-cracks in the μ CT data, rather than indirectly from AE. We used void volume as a metric for void size and estimated inter-void distances (void separation) from the distribution of points defined by ellipse centroids. We obtained void volumes, V_i , and centroids (Text S1b in SI) directly from the Label Analysis module in AvizoTM, and then computed Euclidean lengths, L_i , between centroids.

We obtained maximum likelihood estimates of the void size exponent, β , from the frequency-volume distribution in each μ CT sub-volume. We tested three different but related models often used to describe the seismic moment distribution in seismicity (Kagan, 2002 – full details of this procedure are given in Text S3 in SI):

- (i) GR: the Pareto distribution (a pure power law, equivalent to the Gutenberg-Richter distribution) with cumulative complementary (survivor) function $\Phi(V) = (V_t/V_i)^\beta$ for $V_t < V_i < V_{max}$, where V_i is volume of each individual void and V_{max} is the upper bound (maximum) void volume in the distribution.
- (ii) TRP: the truncated Pareto distribution (similar to the GR but showing a power-law taper in the tail towards V_{max}), with $\Phi(V) = [(V_t/V_i)^\beta - (V_t/V_c)^\beta]/[1 - (V_t/V_c)^\beta]$ for $V_t < V_i < V_c$, where V_c is the tapering corner volume of the distribution.
- (iii) TAP: the tapered Pareto distribution (equivalent to the modified Gutenberg-Richter relation which shows an exponential taper in the tail towards V_{max}), with $\Phi(V) = (V_t/V_i)^\beta \exp[(V_t - V_i)/V_c]$ for $V_t < V_i < \infty$.

We defined a correlation length, $\xi = \sqrt[3]{V_{max}}$ for the pure power-law model or $\sqrt[3]{V_c}$ for the truncated models. The completeness volume, V_t , is the smallest void volume at which 100% of voids in a space-time volume are detected (Rydelek and Sacks, 1989; Woessner and Wiemer, 2005; Mignan and Woessner, 2012), and is equivalent to the threshold of completeness in seismicity data. We obtained V_t from the maximum curvature method (Roberts et al., 2015), i.e., from the peak of the incremental frequency-volume distribution. This method is appropriate for the sharp-peaked distributions seen in our data (Figure S1 in SI). In both samples, the number of voids with $V \geq V_t$ exceeded 200, which is the minimum catalogue size required for reliable estimation of β (Roberts et al., 2015). We used a modified Bayesian Information Criterion (*BIC*) (Leonard and Hsu, 1999; Bell et al., 2013a) to find the most appropriate model (see Text S3 for full details of the calculation, and Figure S2 in SI for the full results) thus obtained the most likely values of β and ξ for each distribution. The *BIC* is

more appropriate for distributions of large sample populations investigated here than the *AIC*, and the results can be compared more directly with previous work (Bell et al., 2013a).

To distinguish the type of phase transition, i.e., whether or not ξ followed an inverse power-law acceleration to failure, we fit the data by non-linear least-squares regression to an inverse power-law model of the form: $y = k(x_p - x)^{-p}$, where x_p is the predicted value of the control parameter x at failure, k is a scaling factor and p parameterizes the rate acceleration of y , all determined by non-linear regression. The point of failure, x_p , is defined by a mathematical singularity as $y \rightarrow \infty$. This is directly analogous to the approach to a critical point in a second order phase transition for the correlation length (Equation 1). It is also equivalent to material failure forecasting approaches based on the Time-Reversed Omori Law for aftershock decay (e.g., Voight, 1988; Cornelius and Voight, 1994; Utsu et al., 1995; Kilburn and Voight, 1998; Kilburn 2003; Smith et al., 2009; Bell et al., 2013b; Vasseur et al., 2015; 2017). We used stress as the control parameter instead of time because the stepped loading procedure that we conducted precludes realistic temporal rate estimates. Importantly, this model makes no *a priori* assumptions about any of the parameters. The predicted failure stress, σ_p , is what would be available in real time, rather than the observed failure stress, σ_c . By estimating σ_p independently, we can quantify any systematic error in its estimation by comparing it to the observed failure stress, and hence quantify any bias in a potential forecasting scenario. We used a trust region algorithm to minimize the residual sum of squares between the observed data and the model (see Text S5 in SI for details). We also tested an exponential model $y = h \exp(qx)$ as an alternate hypothesis. We cannot use a simple criterion such as r^2 alone to determine the relative goodness of fit because the competing hypotheses have different degrees of freedom, so we used the corrected Akaike Information Criterion (*AICc* – see Text S2 in the Supporting Information for details of the calculations). It is based on the residual sum of squares, and is considered more robust than r^2 alone because it takes into account the number of parameters in the model, penalizes models with more parameters and can be used to determine the relative likelihood of the models given the data.

We obtained the two-point fractal dimension, D , from the relation $P(L_i) \sim L_i^{D-1}$ (Turcotte, 1997), where $P(L_i)$ is the incremental probability distribution of the inter-void lengths, L_i (see Text S4 in the SI for more detail). The exponent, $D_{inc} = D - 1$, of $P(L_i)$ in the identified power-law region, $30 < L_i < 1350 \mu\text{m}$, was obtained from a linear regression in log-log space (Figure S3 in the SI). D is then $D_{inc} + 1$. If $D < 3$, voids are clustered spatially but as $D \rightarrow 3$ they become volume-filling, and therefore less clustered (Robertson et al., 1995).

3 Results: Micro-fracture network evolution

Here we present our 4D observations of the evolving segmented fracture network in each sample, together with the distributions of micro-crack orientations. This is followed by results from our quantitative analysis of the fracture network. We first show the influence of heterogeneity on the evolution with strain of (i) stress, porosity and the number of voids, and (ii) void geometry, which reveals how the initial, small anisotropy of the crack network increased in the lead-up to failure. Following this, we test our hypothesis regarding the type of phase transition undergone by each sample by showing the transition to failure of the correlation length as a function of stress. Finally we present the evolution with strain of the correlation length and the scaling exponents of void size and separation. For the purposes of testing our hypothesis and for clarity of presentation we have analyzed data up to failure but not beyond.

3.1 4D observations of micro-fractures and their orientations

The spatial evolution of micro-cracks differs significantly between the two samples (Figure 4 and Figure 5). Although the untreated sample appeared to fail along a localized shear fault (Figure 4P), pre-failure damage accumulated in a spalling pattern of radial damage zones sub-parallel to σ_1 (Figure 4F-O). Conversely, the heat-treated sample failed along a localized shear fault, inclined at 30° to σ_1 , along which pre-failure damage had already accumulated (Figure 5K-P). In both samples, the localized damage zones consisted mainly of shear and axial micro-fractures oriented between 5° and 30° to σ_1 (Figure 6a,b) with bridging ligaments. Local fracture aperture increased as fractures propagated within the localized zones of damage.

In the untreated sample, damage localization (established visually from the segmented CT volumes in Figure 4) first occurred along four narrow zones simultaneously (orange ellipses in Figure 4F) at 1.37% strain and 64% of the failure stress, σ_c , (Table 3). Damage was concentrated along these zones until further radial zones developed on the other side of the sample (pink ellipses in Figure 4J) at 85% σ_c . It is not clear exactly how the eventual fault developed because the sample failed before the next scheduled image time. The post-failure μ CT sub-volume (Figure 4P) indicates that slip occurred along a plane not previously localized and located slightly above where the radial damage had accumulated, which is consistent with the sudden, abrupt nature of the failure inferred from the stress-strain data (Section 3.2.1). However, close to peak stress (97% σ_c ; Figure 4O) cracks had begun to localize along a shear zone that was above and formed from the tip of some of the radial damage zones, and was conjugate to the eventual fault plane.

In the heat-treated sample, damage localization (established visually from the segmented CT volumes in Figure 5) first occurred along a shear zone conjugate to the eventual fault plane (orange ellipse Figure 5H) at 1.24% strain and 72% σ_c (Table 4). Damage progressively concentrated along this plane until localization around the incipient fault plane became apparent (pink ellipse in Figure 5K) at 90% σ_c and 1.38% strain; the same amount of strain as the initial localization in the untreated sample. Fracture nucleation and propagation within the initial damage zone then stopped, continuing instead along this more favorably-oriented zone until failure. This flip in orientation between two optimally-oriented, conjugate, shear planes has previously been seen by Lennartz-Sassinek et al. (2014). Here it coincides with reduced sample stiffness and strain hardening inferred from the stress-strain data (Section 3.2.1).

Microcrack dips, ϕ , became progressively more vertical with increasing stress in both samples (Figure 6a,b), indicating the preferential nucleation of tensile cracks. These cracks formed en-echelon (Tapponnier and Brace, 1976; Kranz, 1979; Olson and Pollard, 1991;

Reches and Lockner, 1994) and wing-crack (Fairhurst and Cook, 1966; Nemat-Nasser and Horii, 1982; Horii and Nemat-Nasser, 1985; 1986; Ashby and Hallam, 1986; Nemat-Nasser and Obata, 1988; Ashby and Sammis, 1990) arrays (Figure 7), concentrated in the heat-treated case at the tip of the propagating fault zone. All radial damage zones in the untreated sample grew in this manner immediately after their initial localization (Figure 4F onwards). In contrast, this process occurred only in the heat-treated sample during localization around the eventual fault plane (Figure 5L onwards), not during the initial localization around the unfavorable conjugate. En-echelon and wing-crack arrays formed at $1.45 \pm 0.01\%$ strain in both samples (Figure 4G and Figure 5L). At this point the untreated sample was only at $70\% \sigma_c$, compared to 90% for the heat-treated sample.

One advantage of the 3D sampling enabled by μ CT imaging is that we can test the null hypothesis that the initial sample porosity is isotropic. The optimal strikes of the segmented voids, θ , show a predominant orientation in the initial porosity in both samples (Figure 6c,d). This starting anisotropy was more pronounced in the heat-treated sample than in the untreated sample ($33.0 \pm 15.1\%$ compared with $14.3 \pm 11.8\%$ - see Table S1 in SI). Overall, anisotropy in the void strike increased steadily throughout deformation in the heat-treated sample but remained approximately constant in the untreated sample (Table S1 in SI). The strike of the eventual fault closely followed this pre-existing anisotropy in both samples, but to a much greater degree in the heat-treated sample. In the untreated sample, although the distribution peaks and troughs broaden as the radial zones localized, the strike of the post-failure fault was oriented within 30° of the initial preferred strike orientation (Figure 6c). In the heat-treated sample, the strike of the emerging fault plane tracked the orientation of the initial crack porosity anisotropy almost exactly (Figure 6d), while the distribution of peaks and troughs remained stationary, and became more defined, as the damage zone localized.

Stereonet depictions (Figure 8) of the void orientations (poles to planes) projected along the axial direction (σ_1) confirm these observations, showing a predominant strike parallel to the pre-existing porosity in both samples, followed by the development of mainly vertical cracks at localization, in line with our visual examination. These cracks initially cluster along the pre-existing strike in both samples but become increasingly distributed in the untreated sample (blue stereonets) during yield and approaching failure, with failure occurring along a fault offset by around 30° to the pre-existing strike. Conversely, in the heat-treated sample (orange stereonets), these vertical cracks cluster increasingly along the pre-existing strike throughout deformation. Closure of some shallow-dipping voids is seen in both samples.

In the time-lapse video of the untreated sample in the x, y projection (Video S1 in the SI), the first axial fracture initiated at a spot on the sample edge close to the bottom of the sample, below and on the outside of a region of concentrated porosity. Further localization occurred simultaneously along vertical zones distributed radially around the sample, which appear to have grown preferentially into the sample before propagating vertically as crack segments linked up. Approaching peak stress, an array of micro-cracks with varying orientations formed around the region of concentrated initial porosity, bridging three radial zones in a curved damage zone. The same process occurred again at $97\% \sigma_c$, bridging four radial zones adjacent to the previous three, but in a conjugate orientation. This bridging fault propagated up the sample (Video S2 in the SI - y, z projection), at a different strike to the post-failure fault.

Time-lapse video of deformation in the heat-treated sample in the x, y projection (Video S3 in the SI) shows that localization initiated within the sample, not at the boundary, on the site of a pre-existing void, precisely as anticipated by Griffith (1921, 1924). Subsequent micro-cracks that localized along the damage zone nucleated between the initial site and the sample

edge. The emerging fault plane initiated at the sample boundary and grew horizontally into the sample, as subsequent micro-cracks localized along it, before propagating down the sample parallel to the z, x plane (Video S4 in the SI – y, z projection). Simultaneously, micro-cracks localized on the opposite side of the sample along the same strike as the initial, arrested damage zone. As deformation continued and the sample reached peak stress, micro-cracks nucleated in the center of the sample. These cracks joined the optimally-oriented damage zone to the conjugate damage zone on the other side of the sample, resulting in a curved shear zone, consisting of arrays of micro-crack segments linked by bridges of intact rock, along which the sample failed.

Accepted Article

Table 3: Differential stress, σ , and axial strain, ϵ , for each μ CT sub-volume in the untreated sample [ACfresh02]. Letters A-P refer to the image volumes shown in Figure 4. Localization first appeared in scan F along several vertical zones distributed radially around the sample. Additional zones localized in scan J but scan P shows that failure occurred along an unrelated shear fault.

ACfresh02	A	B	C	D	E	F	G	H	I	J	K	L	M	N	O	failure	P
σ (MPa)	7	41	60	79	97	116	126	135	144	154	158	163	168	172	177	182	127
ϵ (%)	0.00	0.56	0.81	1.00	1.18	1.37	1.46	1.62	1.71	1.77	1.84	1.87	1.93	1.99	2.08	-	25.79

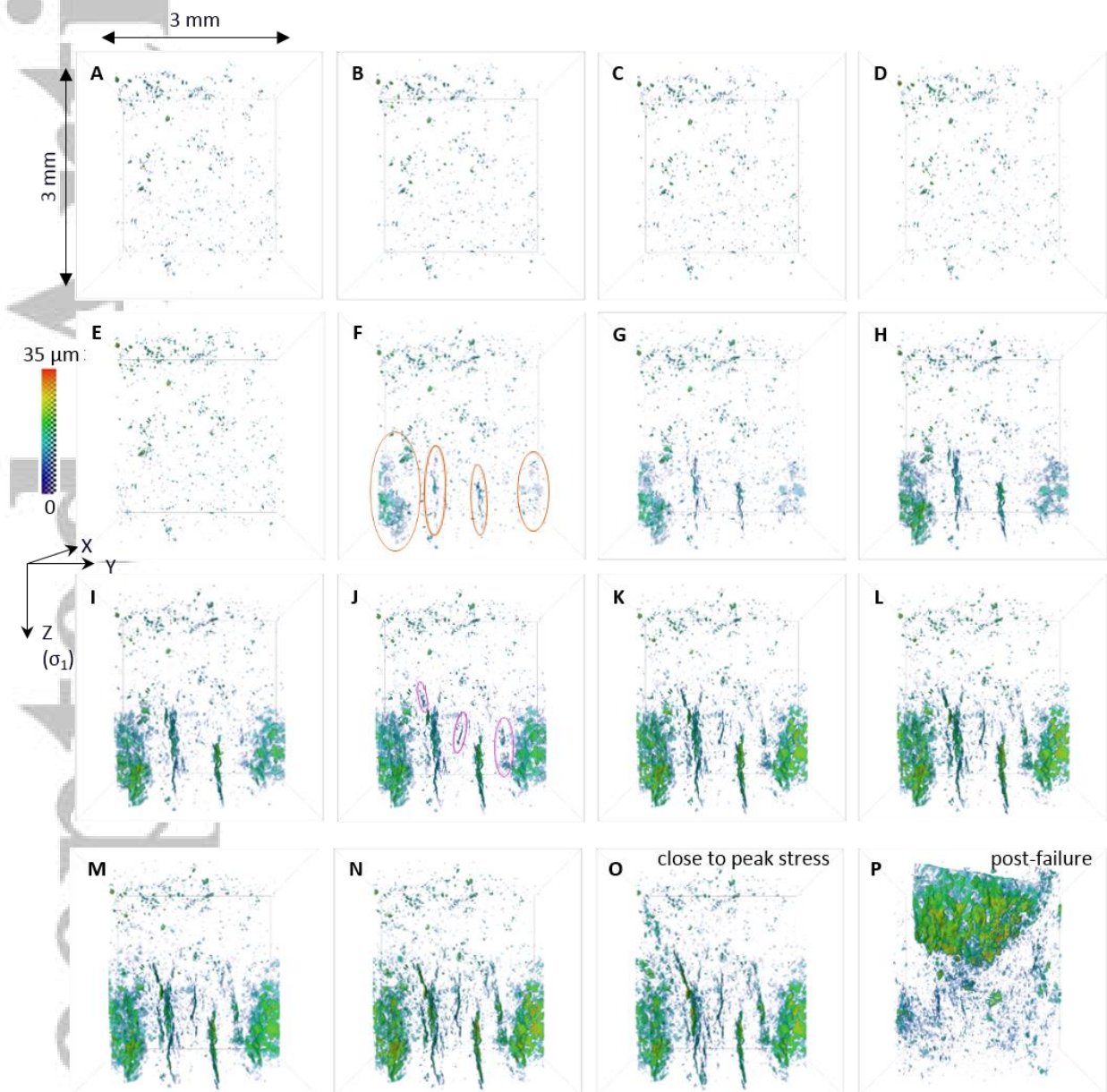


Figure 4: Projection in the y, z plane of segmented microfractures for the untreated sample [ACfresh02]. Orange ellipses show the onset of localization, pink ellipses indicate formation of additional localized zone, completing the radial pattern. Letters refer to the stress-strain steps in Table 3. Color-coding shows the local fracture aperture at each voxel. See Figure S5 in SI for zip file of high resolution images.

Table 4: Differential stress, σ , and axial strain, ϵ , for each μ CT sub-volume in the heat-treated sample [ACHT01]. Letters A-P refer to the image volumes shown in Figure 5. Localization was first seen in scan H along a shear zone that subsequently arrested when microcracks localized along a more favorably-oriented damage zone in scan K, along which the sample eventually failed.

ACHT01	A	B	C	D	E	F	G	H	I	J	K	L	M	N	O (failure)	P
σ (MPa)	7	41	59	78	97	115	125	134	153	162	167	171	176	181	185	102
ϵ (%)	0.03	0.35	0.63	0.84	0.92	1.04	1.09	1.24	1.30	1.38	1.41	1.44	1.53	1.73	1.87	5.65

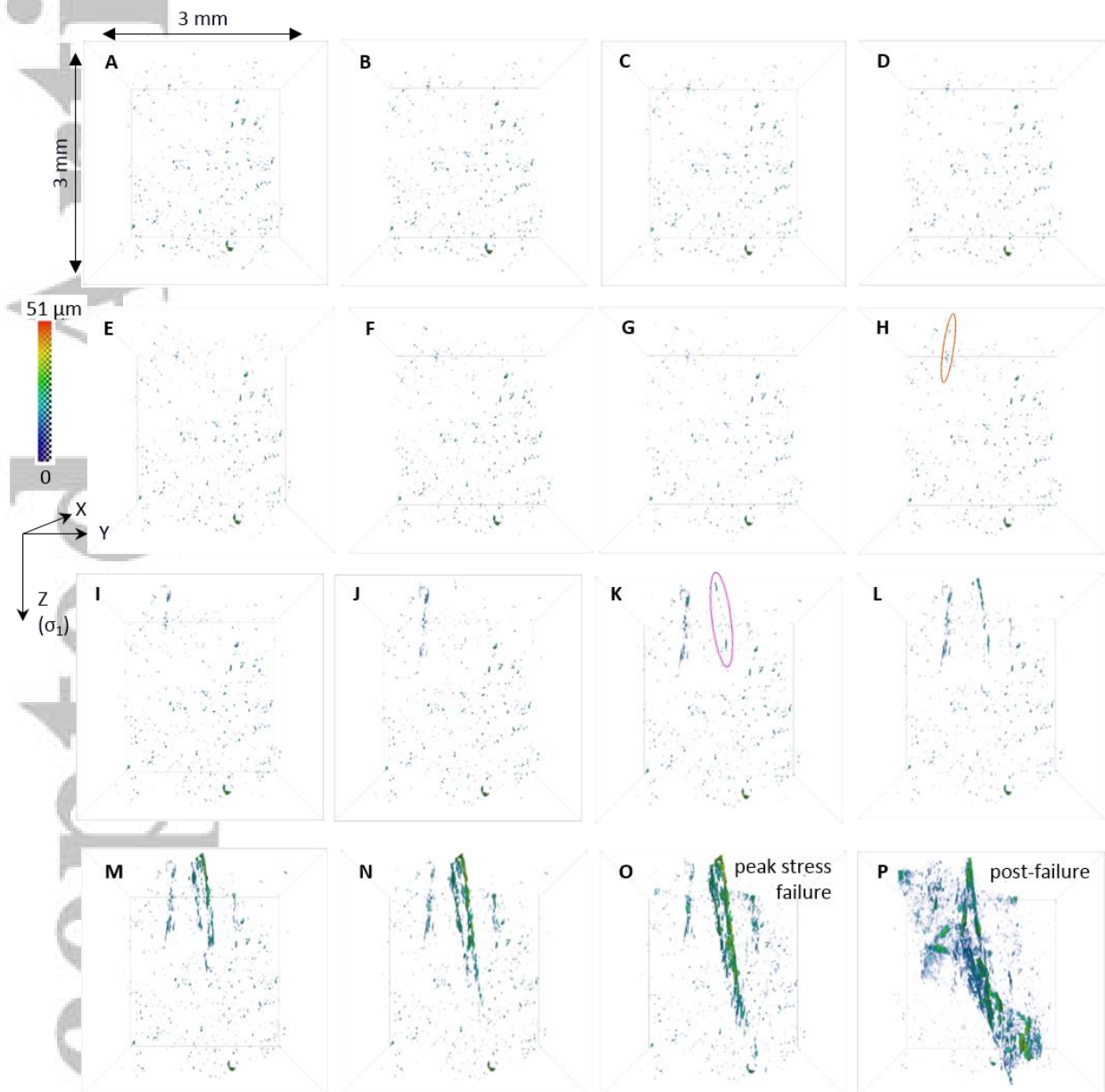


Figure 5: Projection in the y, z plane of segmented microcracks for the heat-treated sample [ACHT01]. Orange ellipse indicates the onset of damage localization, pink ellipse indicates localization along the emerging fault plane. Letters refer to the stress-strain steps in Table 4. Color-coding shows the local fracture aperture at each voxel. See Figure S6 in SI for zip file of high resolution images.

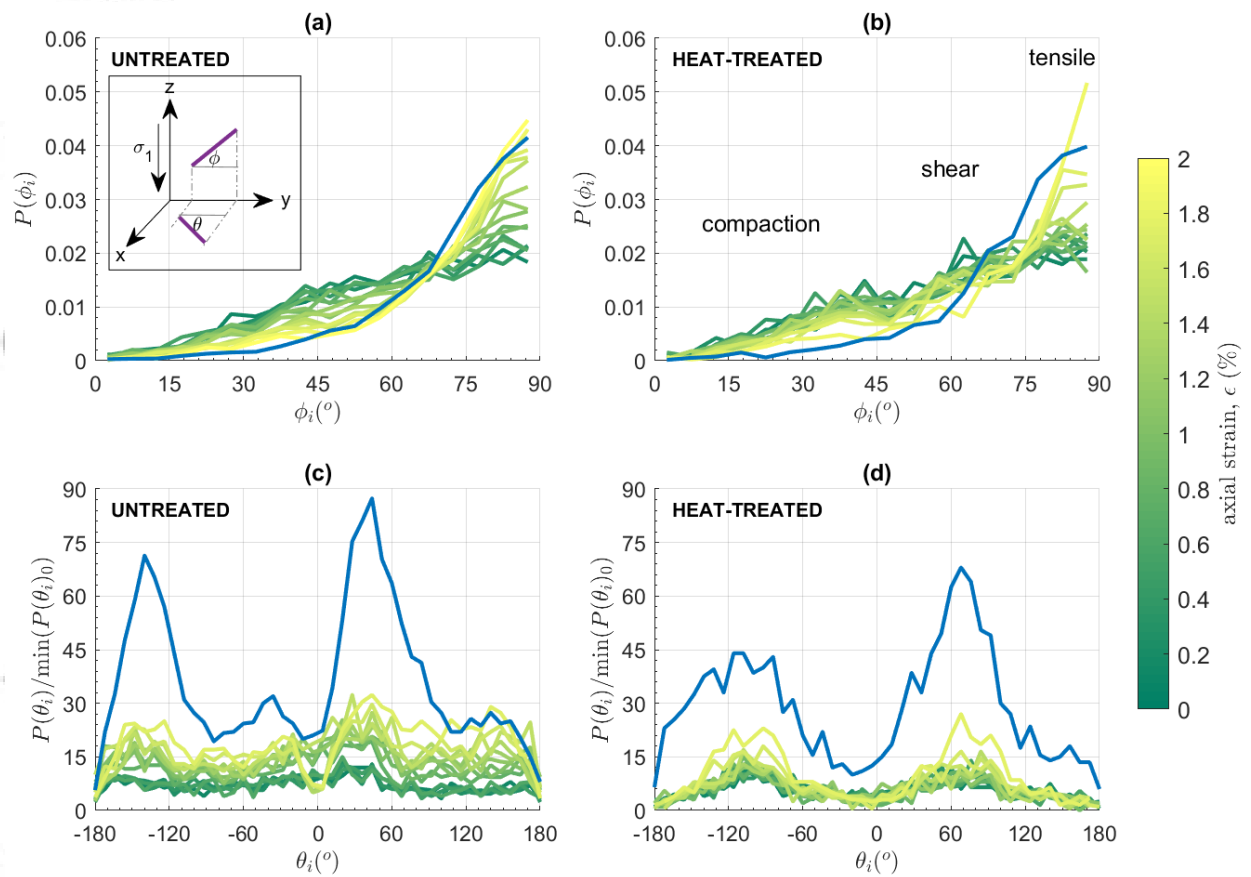


Figure 6: Void (a,b) dip ϕ and (c,d) strike θ probability distributions at each strain increment for (a,c) the untreated sample and (b,d) the heat-treated sample, calculated using the object-based best-fitting ellipsoid approach. Inset shows the measured angles with respect to the principal stress axes: $\phi = 90^\circ$ is parallel to the z-axis, while $\theta = 0^\circ$ is parallel with the y-axis. Labels on the dip distributions show the angles at which different damage mechanisms are prevalent. Strike distributions are normalized to the minimum $P(\theta)$ of the starting porosity. Blue distributions overlaying the rest are post-failure.

Accep

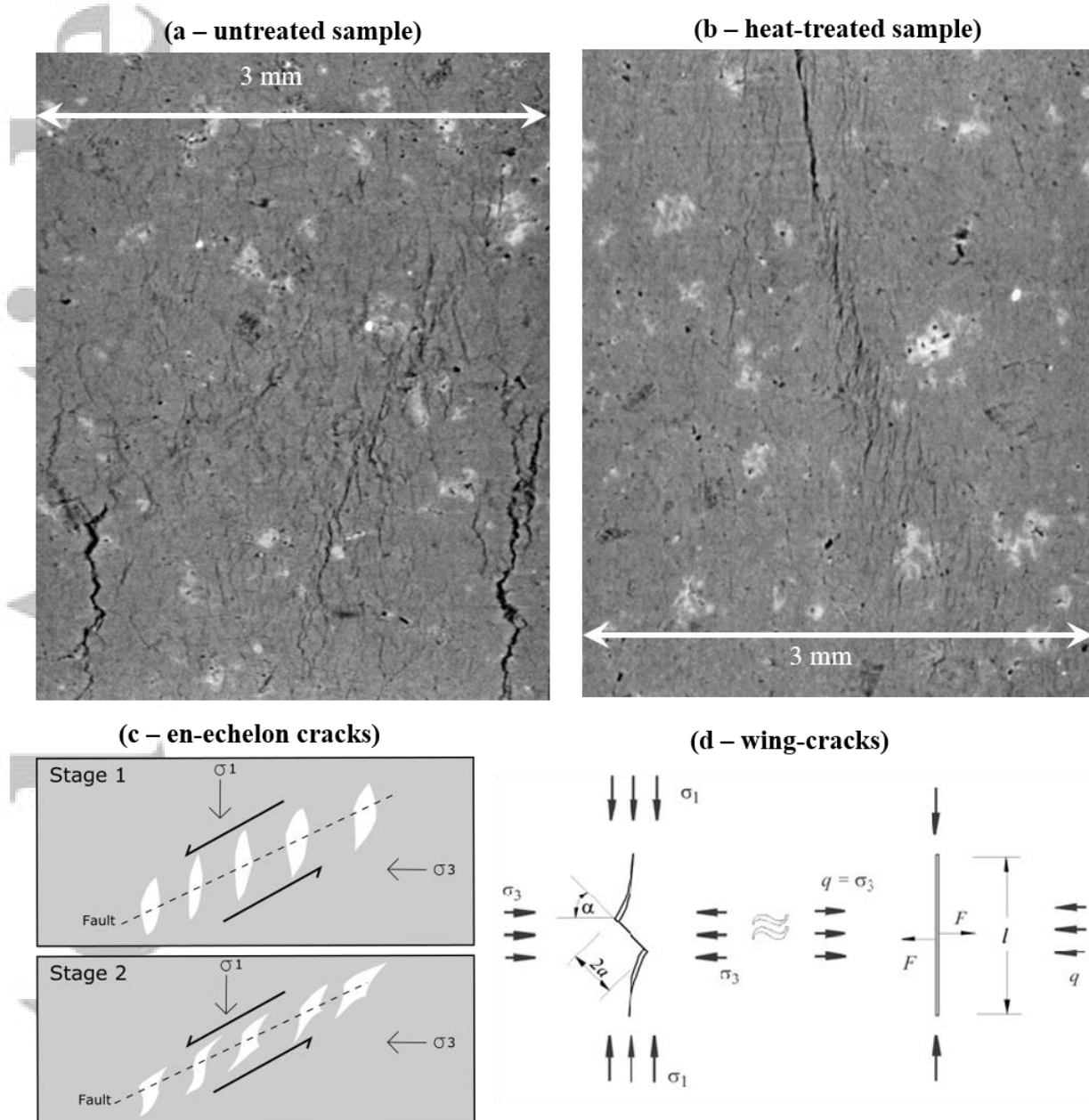


Figure 7: Slice through the sample in the y, z projection showing in (a) the untreated sample close to peak stress (Figure 4O) and (b) the heat-treated sample at peak stress (Figure 5O) the formation of tensile (c) en-echelon (Olson and Pollard, 1991; Thomas and Pollard, 1993) and (d) wing-cracks (Fairhurst and Cook, 1966; Fig. 15 in Damjanac and Fairhurst, 2010).

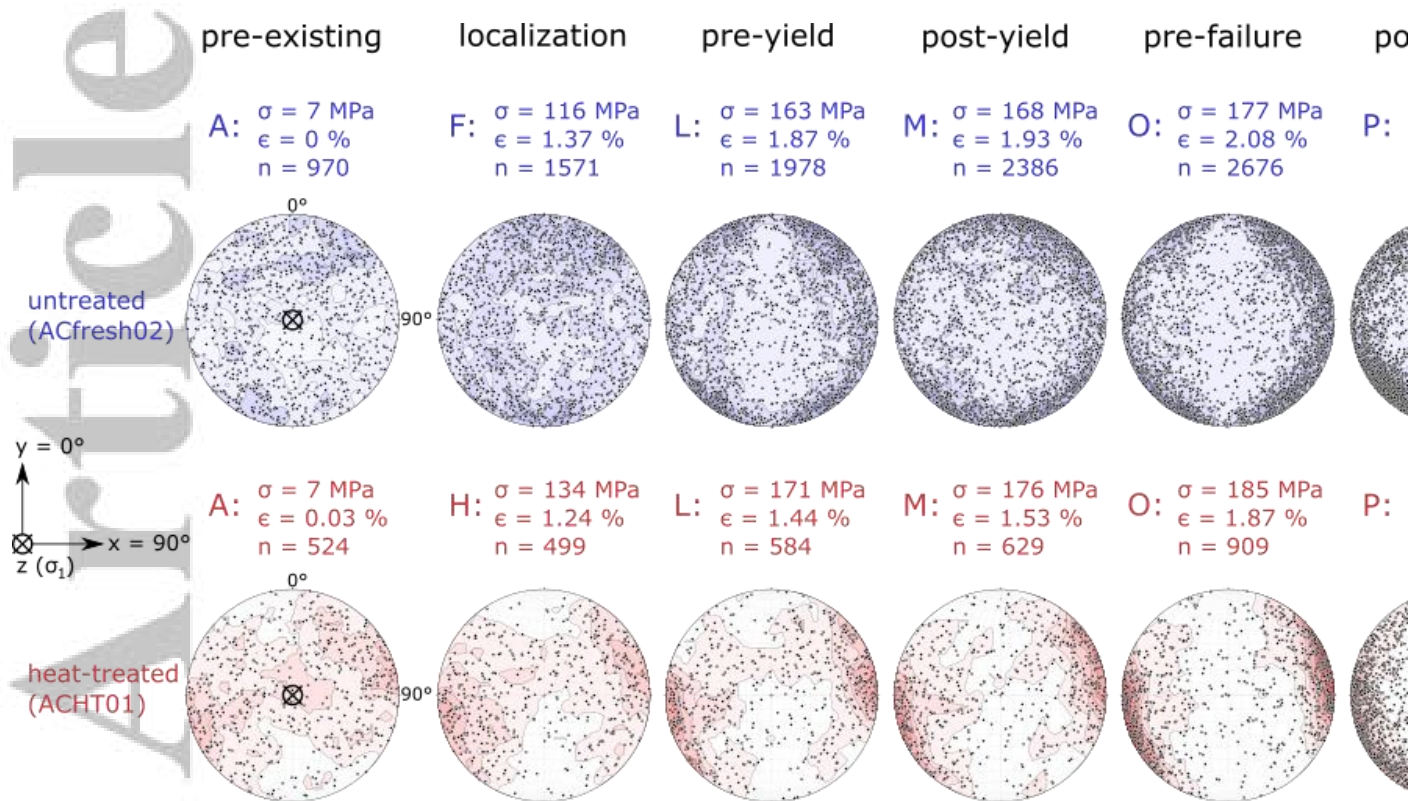


Figure 8: Stereonet projection of void ellipsoid orientations (poles to planes) projected down the loading axis (i.e., in the x, y plane) for both samples. Letters refer to the stress-strain steps for the untreated (Table 3 and Figure 4) and the heat-treated (Table 4 and Figure 5) samples. Clustering contours were calculated from uniform kernel density estimation to show significant departures from a uniform distribution (Kamb, 1959). Kernel radius, $r = 3/\sqrt{\pi(9+n)}$, where n is the number of data points. Contour intervals are given as a multiple of the standard deviation to emphasize the statistical significance of the number of points falling into each kernel (Haneberg, 2004). In the untreated sample, strikes were dominated by the pre-existing porosity until scan F, when micro-crack localization initiated along the steeply dipping, radially distributed zones (orange ellipses in Figure 4). The radial pattern became increasingly symmetrical around the sample throughout the rest of the experiment as these zones propagated and as micro-cracks localized along new zones (pink ellipses in Figure 4). In the heat-treated sample, strikes were dominated by the pre-existing porosity throughout deformation, although the initial localized damage zone observed at scan H (orange ellipse in Figure 5) was conjugate to the eventual fault zone seen at scan J (pink ellipse in Figure 5).

3.2 Evolution of specimen and microcrack characteristics with strain

3.2.1 Stress, porosity and the number of voids

Both samples had a similar stiffness early on (Figure 9a) but the heat-treated sample became stiffer at 0.84% strain when the number of voids decreased slightly (Figure 9c). This is consistent with compaction of the compliant thermal microcracks. The onset of localization, as determined visually from the CT volumes, is evident in both samples as a yield point in the stress-strain curve; at 1.37% strain and 1.24% in the untreated (Figure 4F) and heat-treated (Figure 5H) samples respectively. Further yielding occurred once the damage zone propagated at 95% σ_c in the heat-treated sample (Figure 5M), but only from 97% σ_c in the untreated sample (Figure 4O).

The heat-treated sample had lower pre-existing porosity than the untreated sample ($\varphi_{0\ HT} = 0.62\varphi_{0\ UT}$) and fewer but slightly larger voids ($N_{0\ HT} = 0.54N_{0\ UT}$), with half the number of voids accounting for two-thirds of the porosity seen in the untreated sample (Figure 9b,c). However, this observation only accounts for voids visible above the detection threshold of the segmentation algorithm (a void volume of 3000-4000 μm^3 – see Section 3.3.1), and does not include unresolved nano-scale thermally-induced cracks. The observed differences may be accounted for by natural sample variation within these very small samples and/or some void closure from thermal expansion during the heat-treatment.

Both samples showed a ten-fold increase in porosity, φ , over the duration of their respective deformation experiment (Figure 9b), but only a two-fold increase in the total number of voids, N , in the heat-treated sample, compared with a nearly three-fold increase in the untreated sample (Figure 9c). This indicates that crack nucleation was more dominant in the untreated sample, compared with crack growth in the heat-treated sample. The untreated sample showed no evidence of compaction in the early stages of deformation and the onset of localization (Figure 4E-F) is evident as a large jump in N of 600 voids at 1.37% strain, and a corresponding three-fold increase in φ (Figure 9). Conversely, in the heat-treated sample a small decrease in N of approximately 50 voids provides evidence for some early compaction due to void closure, although this equates to only a tiny proportion (0.005%) of φ_0 . This was associated with the closure of some optimally oriented (shallow dipping) voids prior to localization (Figure 8 – orange stereonet). The onset of localization is evident as a minimum in both φ and N at 1.24% strain (Figure 5H) and both variables exceeded their initial values when the optimally oriented damage zone localized (Figure 5K). Once localization initiated, both samples showed an overall acceleration towards failure in both φ and N . However, in the untreated sample there were two occasions where the acceleration was temporarily arrested. The first of these corresponded to the propagation of new localized zones (Figure 4J), while the second corresponded to the change in orientation of the bridging zone (described in Section 3.1). The heat-treated sample showed a slight slow-down in acceleration that corresponded to the nucleation of new micro-cracks between the two ends of the eventual fault (described in Section 3.1), followed by a final acceleration immediately before dynamic rupture.

In both samples the evolution of both φ and N with strain is best described with simple power-law models (Figure 9b,c); i.e., they have the lowest $AICc$, (Tables S2 and S3 in SI). The exponent is 3.1 for both variables in the untreated sample, compared with 8.8 and 7.7 for φ and N respectively in the heat-treated sample, showing an acceleration towards failure that was almost three times faster in the heat-treated sample than the untreated one. These exponents also show that the acceleration in N accounted for all of the acceleration in φ in the untreated sample, confirming that crack nucleation was the dominant damage mechanism throughout

deformation, whereas in the heat-treated sample, the acceleration in N did not completely account for all of the acceleration in φ , confirming that crack growth played an increasingly important role closer to failure.

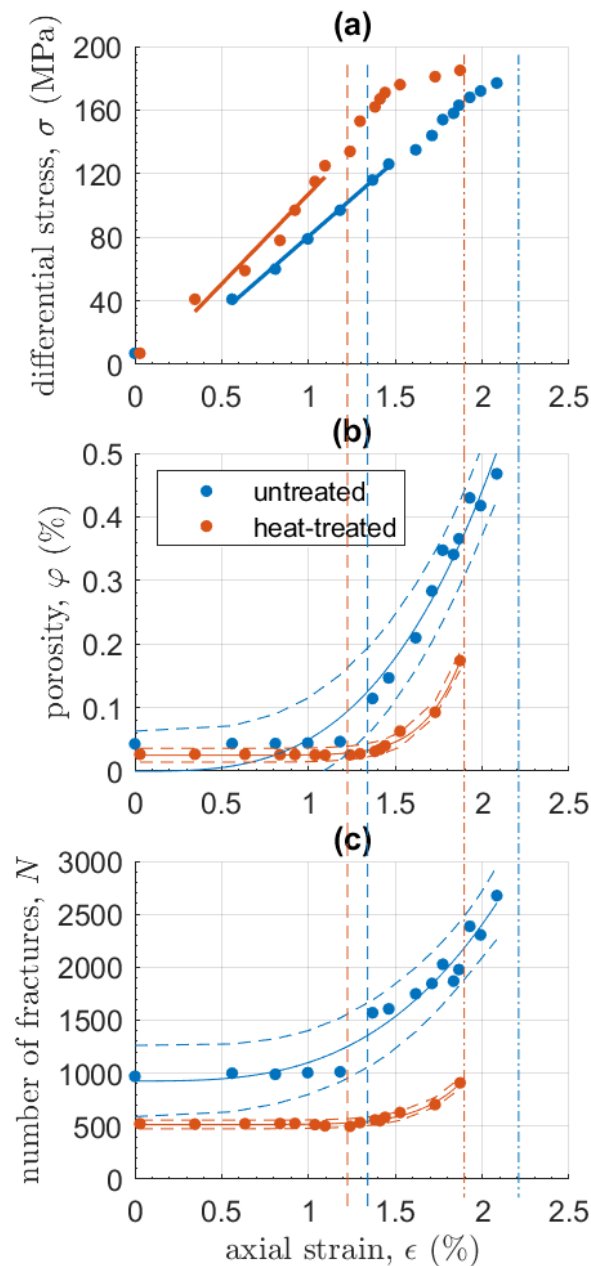


Figure 9: Evolution of (a) differential stress, σ , (b) porosity, φ and (c) the number of segmented voids, N , with increasing axial strain, ϵ for the untreated sample (blue circles) and the heat-treated sample (orange circles). Dash-dot lines show the strain at which each sample failed, while dashed lines show the onset of damage localization as seen the μ CT volumes (Figure 4 and Figure 5). Solid lines in (a) show the region of data used to calculate the Young's moduli (11.3 and 9.5 GPa respectively). Solid lines in (b) and (c) show the preferred simple power-law models with 95% confidence intervals shown as dashed lines; see text for exponents.

3.2.2 Micro-crack geometry

To establish empirically how the micro-crack geometry evolves with increasing deformation, we present the variation with strain of the mean value of the major, minor and medium ellipsoid radii from the population of voids in each μ CT sub-volume (Figure 10a,b). We also show the mean ellipsoid eigenvalue ratios, used to infer the evolution of void aspect ratio (Figure 10c,d). We present two ratios: (i) the smallest to the medium eigenvalue of the covariance matrix (Section 2.5.2 and Text S1b in SI), where flatter objects have smaller values, and (ii) the medium to the largest eigenvalue, where more elongated objects have smaller values.

Corresponding mean void radii, \bar{r} , were about the same size in both samples. In the untreated sample (Figure 10a) \bar{r}_{major} and \bar{r}_{medium} (blue and orange circles respectively) began to increase at the onset of localization (Figure 4F). In the heat-treated sample (Figure 10b) they began to increase as micro-cracks localized along the optimally oriented damage zone (Figure 5K), after the onset of localization. In both samples, r_{major} were oriented approximately parallel to the strike of the eventual fault plane (Figure 6c,d), with their mean values, \bar{r}_{major} , increasing more quickly than \bar{r}_{medium} , showing that micro-cracks grew twice as fast along strike (i.e., perpendicular to σ_1) than down dip, becoming more elongate as deformation progressed (Figure 10c). Voids in the heat-treated sample were marginally flatter than those in the untreated sample, with voids in both samples becoming flatter as failure approached (Figure 10d). This implies that the scaling of crack growth, while scale-invariant in length, may be self-affine (variable aspect ratio) rather than self-similar (constant aspect ratio). The down-dip extent (\bar{r}_{medium}) increased from 2.5 to 4 times the crack aperture (\bar{r}_{minor} – yellow circles). In the heat-treated sample, this was due to continued crack growth down dip relative to a constant crack aperture (Figure 10b). However, in the untreated sample, crack growth down dip stopped altogether close to failure and a small decrease in aperture accounted for the voids becoming flatter (Figure 10a). Growth along strike also stopped (within error), and the continued increase in the number of cracks at this stage (Figure 9c) confirms that nucleation of new cracks accounted for almost all the porosity generation close to failure in this sample.

In summary, the average growth pattern of individual micro-cracks is independent of heterogeneity in the early stages of localization. The behavior changes close to failure, with continued crack growth in the heat-treated sample accounting for the faster acceleration in porosity than void number, while crack growth in the untreated sample was effectively halted in favor of crack nucleation, which accounted for the entire acceleration in porosity and void number as failure approached.

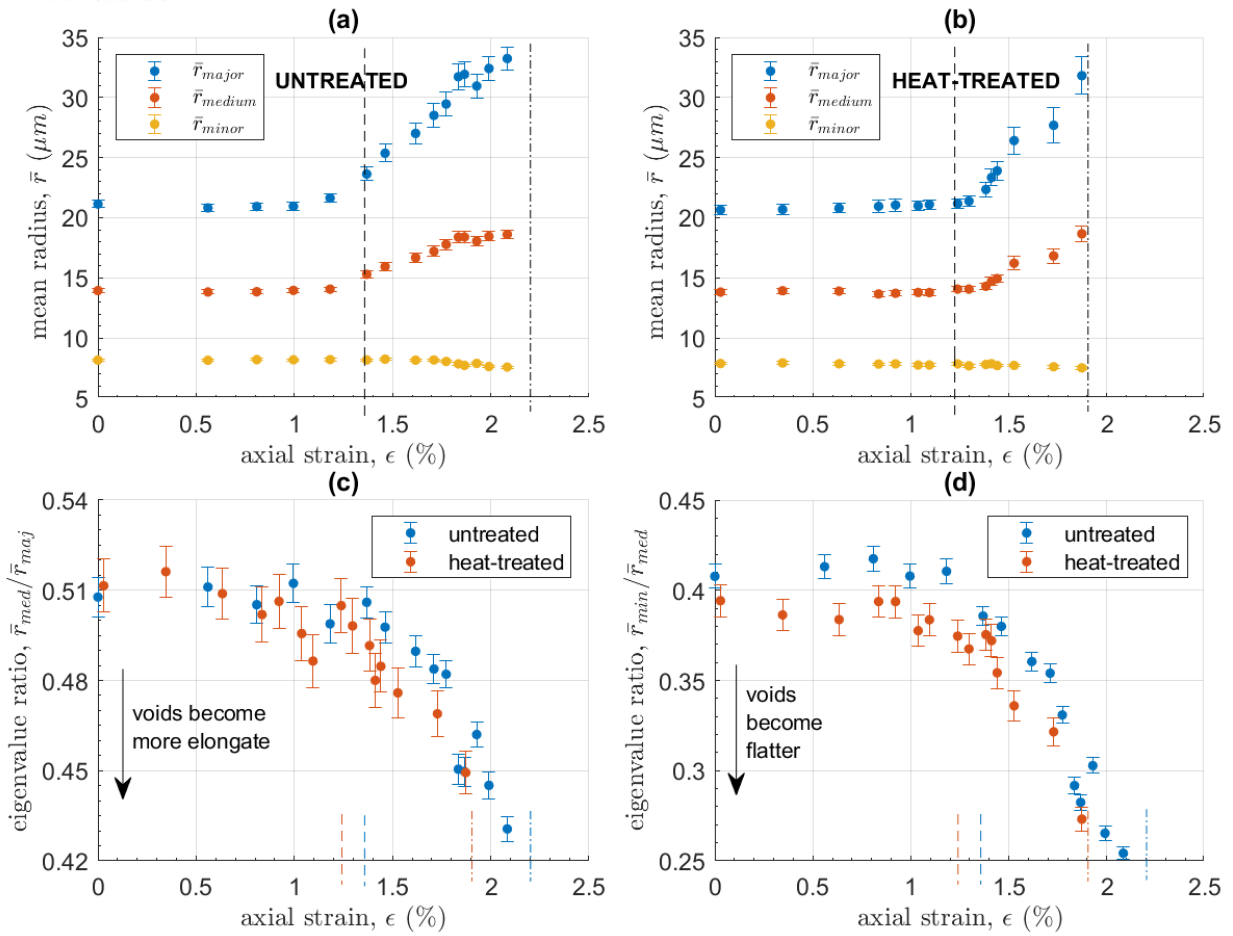


Figure 10: (a,b) Evolution with strain of the mean void ellipsoid radii, \bar{r}_{major} (blue circles), \bar{r}_{medium} (orange circles) and \bar{r}_{minor} (yellow circles), for the (a) untreated and (b) heat-treated samples. (c,d) Evolution of mean void eigenvalue ratios (c) $\bar{r}_{med}/\bar{r}_{maj}$ and (d) $\bar{r}_{min}/\bar{r}_{med}$ with strain in the untreated (blue circles) and heat-treated (orange circles) samples. Voids become flatter or more elongate as the respective ratio $\rightarrow 0$. Error bars show the standard error of the mean in each μCT sub-volume. Dash-dot lines show the failure strain for each sample while dashed lines show the onset of localization as seen in the μCT volumes.

Accepted

3.3 Evidence for phase transition style

To establish the type of phase transition undergone by each sample, we present the evolution to failure of the correlation length and the scaling relations as a function of both differential stress σ and axial sample strain ϵ . Renard et al. (2018) argue that stress is a stronger control variable than strain, but strain is usually the only directly-observable control parameter in real Earth applications. We first present the scaling relationships for void volume and inter-void length, and then show how the correlation length, ξ (linear dimension of the largest void) evolves as a function of stress. We then analyze the evolution of ξ , β and D (the void volume and inter-void length exponents respectively, defined in Section 2.5.3) as a function of strain.

3.3.1 Microcrack volume and inter-crack length distributions

Both samples show an approximately power-law complementary probability distribution in void volume, V_i , (Figure 11a,b), with the proportion of larger voids increasing systematically with respect to strain and stress. Both samples also show an approximately power-law distribution in their inter-void lengths, L_i (Figure 11c,d), within a finite range, identified as $30 < L_i < 1350 \mu\text{m}$ (close to half the sample diameter), with little apparent difference in the shape of the distributions as stress and strain increase. We can therefore define power-law scaling exponents β from the frequency-volume distributions and the correlation dimension D from the inter-void length distributions.

Values of completeness volume, V_t (defined in Section 2.5.3), ranged from 3000 to $4000 \mu\text{m}^3$, roughly equivalent to a void aperture of 14-16 μm . This is much larger than the theoretical detection threshold of half the pixel size (1.3 μm) consistent with under-sampling of very narrow cracks during segmentation. Void volumes in the untreated sample are best described (i.e., have the lowest BIC) by the truncated Pareto distribution (TRP) at the three earliest steps of deformation and then by the characteristic Pareto distribution (GR), with the transition between the two models occurring at 43% σ_c , two stages before the onset of localization (Figure S2 in the SI). In contrast, void volumes in the heat-treated sample are best described by the GR distribution throughout the experiment.

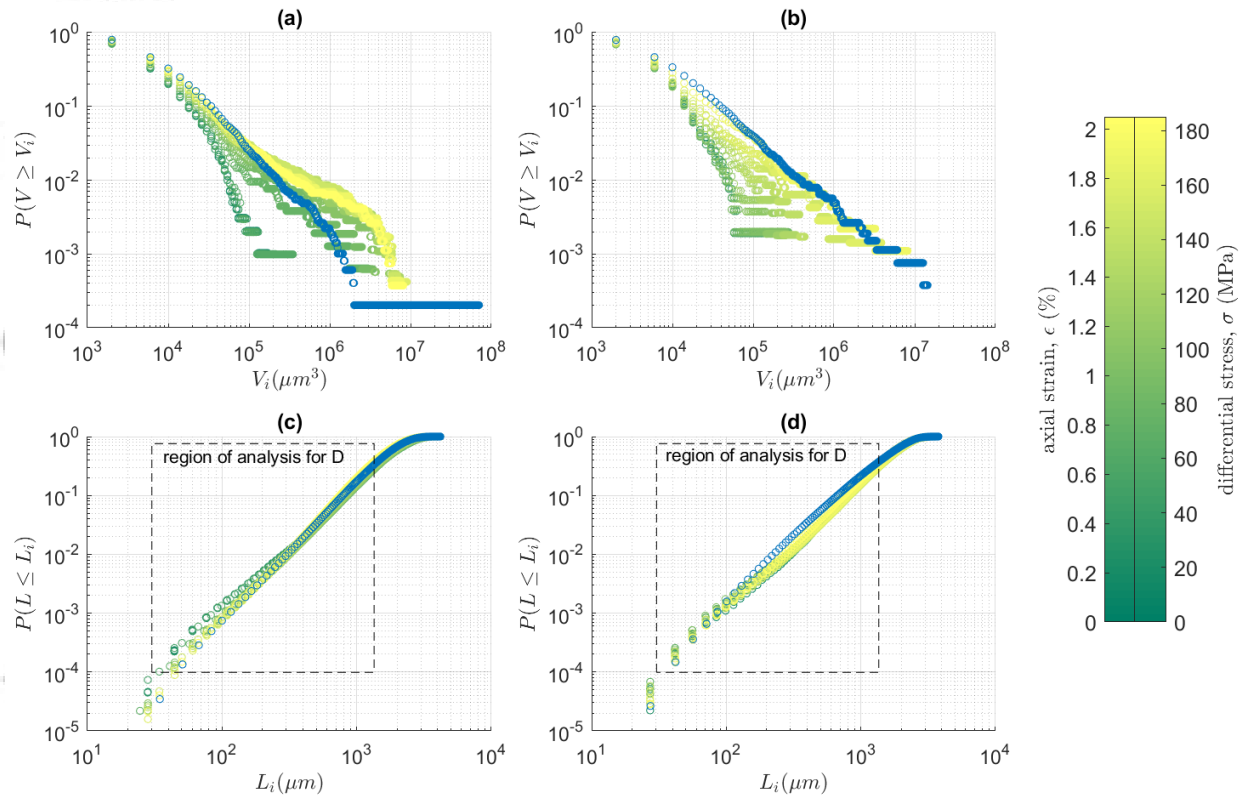


Figure 11: (a,b) Cumulative complementary probability distributions of void volumes, V_i , computed with a bin width of $4000 \mu\text{m}^3$, and (c,d) cumulative probability distributions of inter-void lengths, L_i , computed with 256 bins, at each increment of stress and strain in the (a,c) untreated and (b,d) heat-treated samples. As described in Section 2.5.3, we obtained maximum likelihood estimates for β from the cumulative complementary V_i data (see Figure S1 in SI) using the models of Kagan (2002), and fitted the incremental L_i data using linear regression in log-log space (see Figure S3 in SI) to find D , after Turcotte (1997). Blue distributions overlaying the rest are post-failure.

Accepted

3.3.2 An inverse power-law acceleration to failure?

Parameters for an inverse power-law acceleration to failure for the normalized correlation length, ξ/l , were obtained for both samples (Figure 12), using data observed in segmented μ CT volumes between Figure 4F-O and Figure 5H-O and the method described in Section 2.5.3. While an inverse power-law acceleration is commonly only distinguishable from an exponential acceleration within 10% of the singularity (Bell et al., 2013b), restricting the data to this region (stages L-O in the untreated sample and K-O in the heat-treated sample) would have left very few data points for the analysis. In the untreated sample the exponential and inverse power-law models are indistinguishable over the data range, and the predicted failure stress, σ_p , is far from the observed failure stress, σ_c . The likelihood that the inverse power-law model fits the data as well as the exponential model is just 3% (Table S5 in SI). Thus, it is impossible to define an accurate failure point in this sample. The sample failed abruptly, long before the predicted singularity, after an exponential acceleration in the correlation length. Conversely, in the heat-treated sample, σ_p is accurate to within 3% of σ_c , while the asymptote of the exponential model is further from σ_c . The likelihood of the exponential model fitting the data as well as the inverse power-law is 72% (Table S5 in SI), which although relatively high, is not significant ($>95\%$). These differences are diagnostic of a first (abrupt) and second (continuous) order phase transition respectively (Figure 1), validating our hypothesis that, within the temporal resolution of our experiments, the transition to failure is first-order in the untreated sample and second-order in the heat-treated sample.

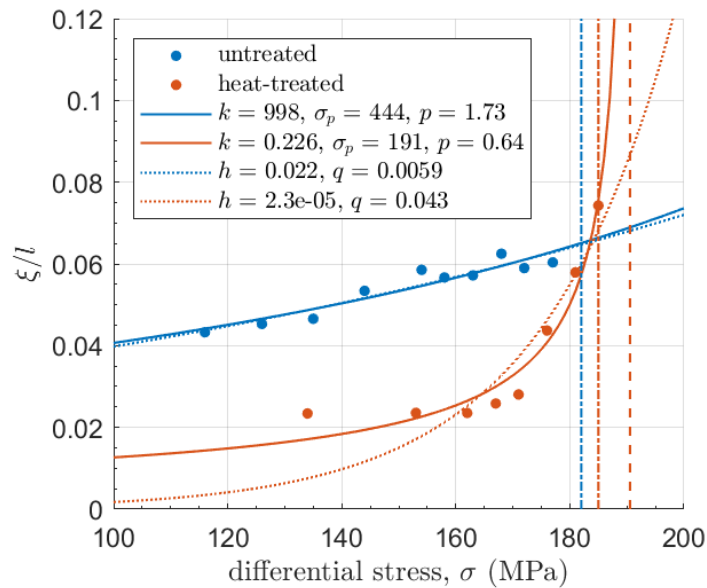


Figure 12: Evidence for an inverse power-law acceleration (solid lines) with respect to stress in the correlation length (normalized by the length of the analyzed sub-volume): $\xi/l = k(\sigma_p - \sigma)^{-p}$ in the heat-treated sample (orange), to a predicted failure stress, σ_p , within 3% of the observed failure stress, σ_c . This compares with the same model yielding a much poorer prediction in the untreated sample (blue), where $\sigma_p = 2.4 \sigma_c$. Dotted lines correspond to the exponential model, $\xi/l = h \exp(q\sigma)$, which in the heat-treated sample is less likely and in the untreated sample is more likely than the inverse power-law model (the relative likelihood of each model is expressed in the main text and also in Table S5 in SI, along with the $AICc$ values). The dash-dot lines show σ_c for both samples and the dashed line shows σ_p for the heat-treated sample.

3.3.3 Evolution of crack population metrics with respect to strain

Both samples show a systematic increase in the correlation length ξ towards failure as a function of strain, with failure occurring when ξ increased beyond 200 μm (Figure 13a). This limit marks the longest crack supported by the sample volume without a runaway instability developing, and falls just short of the mean grain size (i.e., the length between grain boundaries) of the groundmass (250 μm – see Section 2.1). This implies that the sample breaks when whole grains break. The nature of the increase in $\xi(\epsilon)$ in the untreated sample (blue) was exponential (i.e., had the lowest *AICc* – see Table S4 in SI) up to a finite ξ that fluctuated around 200 μm before failure. Conversely, in the heat-treated sample (orange) $\xi(\epsilon)$ preferred a simple power-law acceleration (Figure S4 and Table S4 in SI) to failure, failing when $\xi > 200 \mu\text{m}$. The exponent (6.9) is the same (within error) as the exponents for the evolution of φ and N with strain (Section 3.2.1; Tables S2-S4 in the SI), independently confirming that in this sample crack growth played an increasingly important role closer to failure. The power-law acceleration emerges only once fractures began to localize along the optimally oriented damage zone (at 90% σ_c and $\xi > \xi_0$), representing a strong self-organization in the crack network over all distances to concentrate on the damage zone that controls the eventual fault plane.

The two samples had different initial exponents β for their volume distributions (Figure 13b). In the untreated sample (blue) β rose sharply to a peak at the transition from the TRP to the GR model. This shows that, at this point, the largest cracks in the taper were growing or opening, while simultaneously many more small cracks were becoming active above the segmentation detection threshold. The number of voids and the porosity were constant in this phase, implying other voids were simultaneously closing in compaction (Figure 9b,c). This trade-off is consistent with independent observations from acoustic emissions (Graham et al., 2010) and models (e.g. Brantut et al., 2012; 2014) of the competition between compaction and dilatancy during the quasi-elastic region of the stress-strain curve (Figure 9a). Beyond this peak, β decreased smoothly to the first of two local minima once the additional radial zones had localized (Figure 4K). This indicates instability in the sample-related crack nucleation (Figure 9c and Figure 10a) and might be considered a precursor to failure, albeit without evidence of quasi-static damage zone propagation within the temporal resolution of the method. Conversely, in the heat-treated sample (orange) β decreased throughout, reflecting an increase in the relative proportion of larger micro-cracks. This change occurred gradually at first and then more sharply once cracks localized along the optimally oriented shear zone, similar to that observed in numerical simulations (Kun et al., 2013) and as inferred from AE magnitude distributions (Sammonds et al., 1992) in dry porous media. The sharp drop in β is a clear precursor to failure, corresponding to propagation of the shear zone through the sample (Figure 5M-O). This supports our hypothesis that the heat-treated sample exhibits the clear precursors associated with a second-order phase transition.

The evolution of the two-point correlation (fractal) dimension D was very different between the two samples (Figure 13c). Initially there was a greater degree of clustering in the untreated sample (blue) than the heat-treated one (orange). In both samples D shows a minimum in the two time windows before the onset of localization, demonstrating the sensitivity of D to localization (see also Bonnet et al., 2001). The degree of clustering at this point, reflected in the value of D , was very similar between the two samples. From this point on, D in the untreated sample increased significantly as micro-cracks became more distributed (less clustered) along the radial zones. Conversely, in the heat-treated sample D shows increased clustering that was sustained throughout localization. It recovered (implying decreased clustering) to a relatively constant value as the optimally oriented shear zone propagated stably through the sample before accelerating at the point of failure as the shear

zone spanned the sample. Thus, D highlights clear differences in the spatial distribution of the micro-crack network between the increasingly distributed damage zones in the untreated sample and localization of an asymmetric shear fault in the heat-treated one. The increasingly distributed nature of crack damage in the untreated sample gives no indication of potential failure, while increased clustering due to localization in the heat-treated sample is a clear and early precursor to failure associated with the development of a damage zone optimally oriented to encourage system-sized shear failure. While both samples show precursory changes, only the heat-treated sample has precursors capable of accurately forecasting the point of system sized catastrophic failure.

Accepted Article

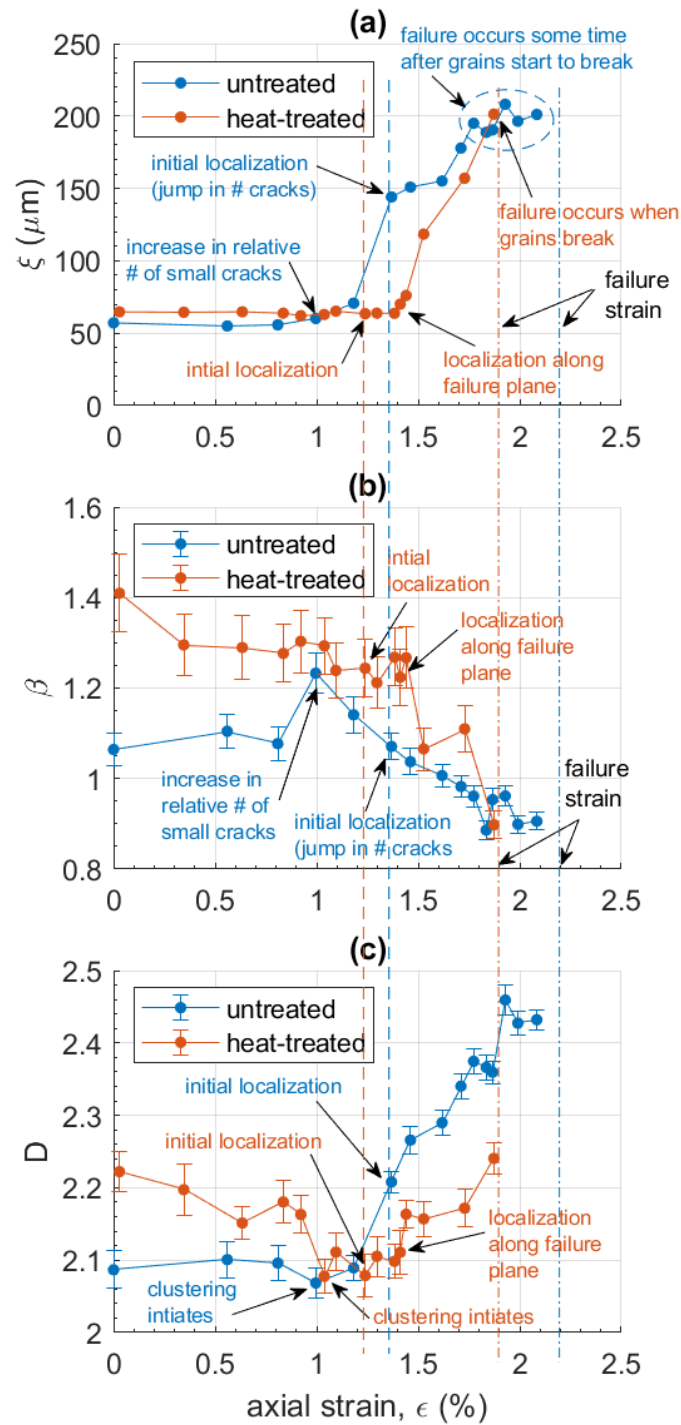


Figure 13: Evolution with strain for (a) correlation length ξ , (b) microcrack volume exponent β , and (c) fractal dimension D , for the untreated (blue) and heat-treated (orange) samples. Error bars show (b) the standard error (β/\sqrt{N}) of the maximum likelihood estimate of β , where N is the number of cracks, and (c) the 95% confidence intervals of the linear regression fit for D . Dash-dot lines show the strain at which each sample failed, while dashed lines show the onset of localization as seen in the μCT volumes.

4 Discussion

The results presented above reveal key aspects of the evolving nature of compressive failure of brittle rocks through the accumulation of micro-cracks that spontaneously organize themselves along localized damage zones. Our synchrotron x-ray micro-tomography (μ CT) observations of *in-situ* compressive rock deformation reveal the underlying processes – in particular the nature of the phase transition between intact and failed states in materials with different degrees of starting heterogeneity. Both our post-failure samples contained a localized shear fault, but the preceding accumulation of micro-cracks was very different between the samples, especially in their spatial distribution and their growth characteristics close to failure. We confirm our hypothesis that, in terms of stress and within the time-resolution of our experiments, the transition to failure is abrupt and unpredictable (first-order) in the homogeneous sample, but continuous and predictable (second-order) in the heterogeneous sample.

4.1 Microcrack network evolution

Prior to failure, our initially crack-free, and therefore more homogeneous, sample accumulated damage in a spalling pattern of localized zones distributed radially around the sample with no preferred strike direction. This damage pattern was completely overprinted during failure, highlighting the drawback of analyzing failed samples retrospectively to gain insights into pre-failure damage accumulation. Pre-failure behavior in this sample resembles strain localization observed from *in-situ* μ CT images of deforming mono-minerallic, fine-grained and uniformly graded (i.e., structurally homogeneous) sand specimens (Desrues et al., 1996). The macroscopic fault localized abruptly at $>97\%$ of peak (failure) stress, σ_c , as microcracks transitioned from being broadly distributed throughout the sample (albeit along several radially oriented zones) to being organized along an emerging shear zone.

In contrast, our pre-cracked, and therefore more heterogeneous, sample accumulated damage around, and subsequently failed along, a localized shear zone. This behavior resembles the observations of Lockner et al. (1991; 1992) who showed progressive localization of AE along a shear zone in deforming Westerly granite samples from peak stress onwards. However, in our experiment the shear zone localized earlier, at 90% of σ_c , with a subsequent period of stable crack nucleation and growth along the damage zone during strain hardening prior to dynamic rupture at peak stress. This behavior resembles fault nucleation and propagation from AE in Berea (Lockner et al., 1992) and Clashach (Liakopoulou-Morris, et al. 1994; Lennart-Sassinck et al., 2014) sandstone samples (arguably more heterogeneous than granite samples in terms of their porosity), where a diffuse damage zone appeared and gradually localized around an incipient fault plane prior to σ_c .

Our results show that heterogeneity exerts a strong control on the evolution of crack network anisotropy, with homogeneity acting to stabilize the system prior to dynamic failure, generating more complex patterns of strain localization with more isotropic global characteristics, as suggested by Desrues et al., (1996). Under axi-symmetric triaxial loading conditions, sample homogeneity is a constraint that favors a transversely isotropic spalling pattern until very close to peak stress, whereas the presence of heterogeneity acts to amplify the pre-existing anisotropy with the formation of a shear fault. Radial spalling patterns are rarely observed in studies of AE, potentially due to limits on their location accuracy, where microcracks occurring along several radially distributed, but localized, damage zones might give the impression of being distributed throughout the sample.

In both of our samples, damage accumulated via the nucleation and sub-critical growth of micro-cracks along localized damage zones. En-echelon and wing-crack arrays formed at

different stages in the deformation process in each sample (at initial localization in the untreated sample but only once the optimally oriented shear zone localized in the heat-treated sample), and formed at the same degree of strain (Figure 4F and Figure 5L), implying a degree of strain control. The main direction of individual micro-crack growth in the localized zones was along strike rather than down dip (Figure 10a,b,c). Models of damage accumulation under tri-axial compression are usually based on AE locations and microstructural observations of post-failure samples, from which it is difficult to quantify the relative proportion of progressive, pre-failure axial to radial micro-crack growth. Along-strike growth is consistent with our conventional tri-axial compressional stress configuration ($\sigma_1 > \sigma_2 = \sigma_3$), in which it is energetically more favorable for tensile micro-cracks to open radially against the axes of minimum principal stress and close against the axis of maximum principal stress. Down-dip fault propagation occurred instead by the nucleation, growth and then linkage of an increasing number of small, tensile en-echelon and wing cracks forming at the fault tip (Figure 6a,b, Figure 7 and Figure 9c). This is consistent with previous experimental and modelling work (e.g., Tapponnier and Brace, 1976; Kranz, 1979; Nemat-Nasser and Horii, 1982; Horii and Nemat-Nasser, 1985; 1986; Sammis and Ashby, 1986; Ashby and Hallam, 1986; Nemat-Nasser and Obata, 1988; Rundle and Klein, 1989; Ashby and Sammis, 1990; Reches and Lockner, 1994; Potyondy and Cundall, 2004; Cho et al., 2007) and recent *in-situ* observations of damage accumulation in strong rocks (Renard et al., 2017; 2018).

We observed significant anisotropy of void strike in the pre-existing porosity in both samples (Figure 6c,d), despite visual inspection of thin sections and compressional wave velocities of the same rock type showing only 1% anisotropy in bench-top tests on the original material (Meredith et al., 2005; Meredith, pers comm.). This indicates that a small velocity anisotropy represents substantial void anisotropy. The pre-existing void anisotropy is more pronounced in the heat-treated sample than in the untreated sample, possibly due to thermal expansion during the heat-treatment acting to close the isolated, mainly round voids in the feldspar micro-phenocrysts (Meredith et al., 2012). This may also account for the otherwise counter-intuitive smaller overall porosity in the heat-treated sample compared with the untreated one. The application of confining pressure may also have contributed to the porosity difference by acting to close the thermally-induced cracks in the heat-treated sample more effectively than the stiffer pores in the untreated sample. In the heterogeneous sample, the preferred strike of the pre-existing porosity corresponds almost exactly to the strike of the emerging fault plane (Figure 6d). There was also significant amplification of the pre-existing anisotropy of the rock fabric (from 33% to 96% just before failure; Table S1 in SI). This was not the case in the homogeneous sample, where the degree of anisotropy remained approximately constant throughout the lead-up to failure (Table S1 in SI), consistent with the lack of an overall preferred strike in the pre-failure localized zones in this sample.

The results in the previous paragraph prove that the initial microstructure, specifically the orientation and anisotropy of pre-existing porosity dictated the geometry and location of the future (post-failure) fault, particularly in the heat-treated sample. We speculate that this happens via a modification of the local stress field with respect to the principal stress axes. In true tri-axial configurations ($\sigma_1 > \sigma_2 > \sigma_3$), shear wave velocity anisotropy measurements have shown that micro-cracks in general propagate parallel to σ_2 as they open parallel to σ_3 (Crawford et al., 1995), while polymodal faulting is also often seen (Healy et al., 2015). Thus, although the global stress configuration is axi-symmetric in our case, both heterogeneity and void anisotropy in the microstructure appear to cause the local development of truly tri-axial stresses such that a particular strike is preferred. One possible mechanism for this may be stress rotation around microstructural discontinuities (Faulkner et al., 2006), possibly reflected in our experiments in the rotation of the void ellipsoids with respect to the principal stress axes (Figure

6c,d). In this case, the pre-existing network of anisotropic micro-cracks with a preferred orientation would have generated an emergent, locally dominant true-triaxial stress field within the body of our heterogeneous sample, even though the confining pressure was isotropic around the vertical (σ_1) axis. Conversely, in our homogeneous sample, some complex interplay between local true tri-axial stresses and global axi-symmetry would be required to generate several radially distributed damage zones simultaneously. We speculate that the global axi-symmetry initially counteracts the rotation of internal stresses in this sample, acting to prevent an increase in crack anisotropy and thereby increasing the uniformity of the strike distribution as the experiment progresses. Thus, the relationship between the evolving anisotropy of the micro-cracks and their preferred orientation is likely to be a controlling factor on the geometry and location of an asymmetric shear fault, on the timing of the formation of this fault and on whether pre-failure damage is localized along this fault or not.

In both our samples, the majority of cracks dip steeply within $\pm 15^\circ$ of the loading direction, although a few dip less steeply between 15 and 30° (Figure 6a,b). This is consistent with the results of post-failure sample analysis in early experimental work (Brace et al. 1966; Hallbauer et al. 1973; Lajtai 1974). The macroscopic fault in our homogeneous sample dips at a similar angle to the pre-failure micro-cracks, whereas in our heterogeneous sample it dips less steeply post-failure than it does at peak stress. Although the effective pressure was relatively low (15 MPa), which may promote axial failure over shear, it was consistent across the two experiments. This implies that the differences in fault dip result from an intrinsic microstructural response, whereby the emergent internal friction coefficient decreases during failure in the heterogeneous sample but remains constant in the homogeneous sample, consistent with DEM models (Kun et al., 2018) that show a decreasing coefficient of internal friction with increasing heterogeneity. In both samples, the dip angle increases during quasi-static damage accumulation, increasing earlier in the homogeneous case (during initial localization) than the heterogeneous case (only during localization around the optimally oriented shear zone). In the homogeneous case, the steep dip of the nucleating cracks (Figure 6a and Figure 7a) and the eventual fault plane (10° ; Figure 6a) indicates that the internal friction coefficient in this sample is sufficiently high to inhibit micro-crack damage by shear mechanisms until immediately before dynamic failure. In the heterogeneous case, the dip, and therefore the internal friction coefficient, increases only during propagation of the shear zone and is particularly pronounced immediately before failure (Figure 6b), while the eventual fault plane dips less steeply (30° ; Figure 6b). This indicates that early crack nucleation and failure itself both involve shear mechanisms, but shear zone propagation is governed primarily by tensile mechanisms, i.e., the accumulation of en-echelon tensile cracks (Figure 7b), with a corresponding increase in the internal friction coefficient. For this reason we have referred to a ‘damage zone’ prior to failure and a ‘fault plane’ afterwards.

In our homogeneous sample, increased clustering (Figure 13c; blue circles) occurred at 43% σ_c with the onset of localization at 64% . This agrees with observations and models of cracks initiating earlier than the theoretical shear-sliding threshold for more homogeneous low porosity, crystalline rocks (70% σ_c ; Hallbauer et al., 1973; Nicksiar and Martin, 2013; 2014). The implication is that our more homogeneous sample is weakest in tension and, once a sufficient number of tensile cracks form, a macroscopic shear fracture will naturally develop. We therefore conclude that damage in this sample most likely initiated via the nucleation of pore-emanating (Sammis and Ashby, 1986; Ashby and Sammis, 1990) or force-chain controlled (Potyondy and Cundall, 2004; Cho et al., 2007) tensile micro-cracks due to the redistribution of stress around equant compressing pores and grains. Conversely, increased clustering in our heterogeneous sample (Figure 13c; orange circles) occurred at 62% σ_c with the onset of localization at 72% . This is later than the theoretical shear-sliding threshold for

heterogeneous rocks (60% σ_c ; Hallbauer et al., 1973; Nicksiar and Martin, 2013; 2014). The implication here is that our more heterogeneous sample is weaker in shear than in tension since shear sliding along preferentially oriented, pre-existing cracks occurred before tensile cracking. We therefore conclude that damage in this sample most likely initiated via the development of tensile ‘wing-cracks’ (Nemat-Nasser and Hori, 1982; Horii and Nemat-Nasser, 1985; 1986; Ashby and Hallam, 1986; Nemat-Nasser and Obata, 1988; Ashby and Sammis, 1990) at the tips of pre-existing defects due to shear-sliding along those defects. Unfortunately, such shear sliding would not be visible in our images without significant dilatancy during slip.

In summary, our experimental data confirm that the initial heterogeneity within a rock sample is a key control over how cracks, pores and grain boundaries interact locally with the applied stress field, and imply that the microstructure transitions from being weakest in tension to being weakest in shear as heterogeneity increases.

4.2 Scaling, phase transition style and predictability of failure time

Micro-crack volume and inter-crack length distributions follow power-laws throughout the cycle of deformation and failure in both samples, characteristic of the scale-invariant (fractal) nature of natural fault networks (Main et al., 1990; Bonnet et al., 2001) and consistent with the power-law microcrack volume distributions observed by Renard et al. (2017; 2018). The transition from the TRP to the GR model for the micro-crack volume distributions (Figure S2 in SI) in the homogeneous sample emulates changes in the organization of earthquake size distributions following the occurrence of extreme or very large earthquakes (Bell et al., 2013a). Close to failure the void volume distribution shows a bump at large volumes, indicative of a supercritical state with an elevated probability of occurrence of large events (Main, 1996), sometimes known as ‘dragon kings’ (Sornette, 2009). We have demonstrated that the parameters of these distributions are more sensitive to heterogeneity than porosity alone, consistent with the findings of Vasseur et al. (2017) and Kun et al. (2018). In combination with μ CT observations of fault formation, the evolution of these parameters provides a microstructural explanation for the variation in the systematic prediction error for the failure time based on acoustic emissions (Vasseur et al. 2015).

However, the systematic change in the mean void aspect ratios during crack growth may indicate that the scaling of crack growth is self-affine (i.e., exhibits scale-invariance in length with different exponents for individual growth axes, leading to a variable aspect ratio) rather than self-similar (the same scaling exponent for all growth axes, with a constant aspect ratio). This is consistent with observations of fracture surface geometries in rocks (Schmittbuhl et al., 1995) and other materials (Mandelbrot et al., 1984; Bouchaud et al., 1990; Russ, 1994; Schmittbuhl and Maloy, 1997; see also Bouchaud, 1997 for a review), which are well-described by self-affine fractals. These studies have shown that scaling along the aperture axis is systematically smaller than along the mean crack plane, with the systematic (Hurst) exponent defining the fracture roughness (Bouchaud, 1997; Weiss, 2001). Our observation that almost no growth at all occurs along the aperture axis supports the conjecture that the aperture direction is not physically equivalent to the mean crack plane (Schmittbuhl et al., 1995). Our results indicate that scaling along the strike and dip axes may also systematically differ from each other. This contradicts the notion of strict self-similarity in the mean crack plane (Schmittbuhl et al., 1995), and implies that the strike and dip directions are not physically equivalent either. Further work is required to quantify the scaling anisotropy for crack growth in our experiments and to test these hypotheses. Since crack surfaces in crystalline materials require heterogeneities, such as grain boundaries and dislocations that pin the propagating crack front, in order to develop self-affine roughness (Schmittbuhl and Maloy, 1997;

Bouchaud, 1997; Weiss, 2001), we expect that scaling exponents for the heterogeneous sample may be more anisotropic than for the homogeneous sample.

In the heterogeneous (heat-treated) case, we find evidence for a continuous (second-order) phase transition in the inverse power-law acceleration to failure of ξ with respect to stress (Figure 12; solid orange line), with failure occurring near the asymptote, together with clear precursors in β and D . The rapid decrease in β corresponds to the formation of a localized damage zone optimally oriented for macroscopic shear failure, occurring when the microcrack network self-organizes. This provides a clear precursor to sample failure related to a distinct physical process, i.e. the emergent inverse power-law acceleration in ξ . The asymptote defines a predictable failure time defined by a smooth transition to an infinite ξ at the sample-scale (Figure 1; orange line). The early and sustained decrease in D in 3D is a key precursory indicator of localization, while its recovery is associated with shear zone propagation in 2D, as anticipated by the model of Main (1992). This provides another clear precursor to failure. Such behavior agrees with statistical physics models of rupture as a critical, second-order phenomenon (Girard et al., 2010; Kun et al., 2013). Thus, taken together, these variables show that damage localization along a zone optimally orientated for macroscopic shear failure is the physical process that defines whether the phase transition from an intact to a failed state is second-order, and therefore predictable, with reliable precursors to failure.

In the homogeneous (untreated) case, we find evidence for an abrupt or discontinuous (first-order) phase transition, with an unsuccessful forecast of the failure stress, and a preference for an exponential model for the evolution of the correlation length, ξ , with respect to stress. Furthermore, there is very little evidence for reliable precursors in either the microcrack volume exponent, β , or the two-point fractal dimension, D , and the bump in the void size distribution at large volumes is reminiscent of a first-order phase transition (Lomnitz-Adler et al., 1992; Ceva and Perazzo, 1993). Approaching failure we see small fluctuations in β , ξ and D that may indicate impending failure as they are associated with formation of the additional damage zones and subsequent microstructural instability due to crack nucleation close to failure. However, using these parameters as precursors may lead to false alarms since they are not associated with the eventual fault plane. The exponential increase in ξ (implying that local correlations dominate) is unusual and generally associated with the critical regime during phase transitions across surfaces (Kosterlitz and Thouless, 1973; Kosterlitz, 1974), such as during large-scale faceting at the surfaces of growing crystals (Nozières, 1992). Its stabilization to a finite value shortly followed by abrupt failure is characteristic of a first order phase transition (Figure 1; green line). In numerical models of fault growth, an exponential distribution of fault lengths is associated with crack nucleation, whereas a power-law distribution emerges with nucleation plus crack growth and coalescence (Cowie et al., 1995). Hence, the origin of this response in our rock volume may be explained by our observation that crack nucleation is the dominant damage process in the homogeneous sample while crack growth becomes increasingly important closer to failure in the heterogeneous sample (Section 3.2.1). This behavior corresponds to the existence of a metastable state of crack nucleation at a system-sized ξ during a first-order transition, when the system is vulnerable to the influence of sufficiently large perturbations (subcritical bifurcation) (Sornette, 2006). This vulnerability and the resulting discontinuity may be the reason for an unpredictable failure time (Vasseur et al., 2015).

An estimate for the correlation length exponent (1.15) for Carrara marble (Kandula et al., 2019) falls almost exactly halfway between the exponents for Ailsa Craig microgranite found here (0.65 for the heterogeneous sample and 1.75 for the homogeneous sample). However, the Carrara marble exponent was estimated by assuming the failure stress *a priori*, so it is not directly comparable with our results. It is therefore not possible to confirm whether

an inverse power-law would successfully forecast the failure stress in real time and/or whether a different model would be more likely. Nevertheless, the nature of Carrara marble may place it halfway between our two end members. It is chemically pure, composed of 99% annealed calcite crystals (Alber and Hauptfleisch, 1999), with a homogeneous microstructure (Oesterling, 2004), a very low permeability (10^{-19} m²) and only 0.2-0.5% connected porosity (Zhang, 1994; Alber and Hauptfleisch, 1999; Bandini et al., 2012; Cartwright-Taylor et al., 2015). However, studies have shown the presence of micro-discontinuities within grains, including twin lamellae (Ramez and Murrell, 1964; Bandini et al., 2012; Cartwright-Taylor et al., 2015) and a high density of dislocations (Fredrich et al., 1989), while its isotropic texture consists of both well-locked (xenoblastic) and more mobile (granoblastic) grain boundaries (Bandini et al., 2012; Cartwright-Taylor et al., 2015). These factors indicate a complex history of both static and dynamic recrystallization (Molli and Heilbronner, 1999; Oesterling, 2004) and introduce a degree of heterogeneity that may be intermediate between our two samples.

In both samples, the critical value of ξ is 200 μm , marking the longest crack supported by the sample volume without a runaway instability developing. Significantly, this falls just short of the mean grain size of the groundmass (250 μm). That is, catastrophic failure occurs when whole grains break. This confirms the findings of Vasseur et al. (2017) from acoustic emissions (AE) data that the grain size (inter-particle distance) is a better metric for the characteristic void dimension at failure than the distance between pores (inter-void distance).

Our observations highlight the strong dependence of the degree of predictability on material properties that may be unknown in a field application, as well as the importance of analyzing several independent parameters for identifying the type of phase transition and predicting the point of failure (Lei and Satoh, 2007). They may also explain why, when looking at long time-series of field-scale seismicity or deformation, clear and reliable precursors to failure are detected only in some cases, and preferentially in application to forecasting of landslides and volcanic eruptions. In other cases, notably in forecasting of individual large earthquakes, fluctuations related to instability may be present but may not be statistically significant enough to be detectable as precursors. In both samples, D shows increased clustering earlier than localization is visually apparent in the μCT images, and therefore may provide useful information about the impending onset of damage localization for a variety of applications and settings. Finally, the relatively high strain rates analyzed here may not be representative of the evolution of precursors at lower strain rates. For example Ojala et al. (2004) showed that the acceleration to failure in AE rate asymptotically approaches the behaviour expected of a single Griffith crack (Figure 1) as strain rate is decreased in laboratory compression tests on porous sandstones. Nevertheless, we have confirmed that heterogeneity plays a significant role in determining the style of evolution of the population of micro-cracks, and hence the predictability of the system-scale failure time.

4.3 Suggestions for future work

This discussion has highlighted some outstanding research questions to be addressed in future work. The most notable of these are as follows: (i) Why do previously obtained degrees of anisotropy inferred from acoustic measurement differ markedly from our newly obtained structural ones? (ii) How does crack growth scale (in terms of the ellipsoid radii), and is it self-affine? (iii) Does the predominant local failure mechanism change from tensile to shear as system-sized failure approaches, as seen in the AE data of Graham et al. (2010)? (iv) Does this transition occur earlier in more heterogeneous materials? Given tensile fractures are easier to see in imaging void space, the latter two questions would benefit from digital volume correlation techniques that are the subject of ongoing work, and can detect local changes in shear and volumetric strain.

5 Conclusions

Our *in-situ* time-resolved x-ray μ CT images of very small samples of deforming granite show that the heterogeneity of the starting material exerts a strong control on the evolution of the statistical properties of crack size and spatial distribution during fracture network evolution. The accumulating micro-cracks have power-law frequency-volume and inter-crack length distributions over a finite scaling range, irrespective of the degree of starting heterogeneity, with well-determined scaling exponents β (the size exponent) and D (the correlation dimension). The inferred correlation length ξ increases exponentially with respect to stress in the homogeneous case, with sudden-onset, unpredictable failure, analogous to the behavior expected for a first-order (discontinuous) phase transition. In contrast, the heterogeneous sample shows an inverse power-law acceleration to a predictable failure point at the asymptote, diagnostic of a second-order (continuous) phase transition (Equation 1 and Figure 1). The second-order transition is linked to the distinct physical process of quasi-static, asymmetric accumulation of damage within an optimally-oriented zone increasingly localized around the eventual fault plane, with associated reliable precursors to failure in the evolution of β and D . The correlation dimension is a key early indicator of localization on such a shear zone for the heterogeneous sample. This is not observed within the time resolution of our observations for the homogeneous sample, where the precursory damage takes the form of more radially isotropic zones of spalling, and shear localization must occur very close to the point of dynamic failure itself to explain the post-failure observation of a shear fault.

Crack nucleation dominates the frequency-size statistics in the homogeneous case and crack growth in the heterogeneous case. In both cases, the transition to localized damage occurs by a combination of nucleation and growth. The timing of the onset of crack coalescence defines the order of the phase transition, and hence the predictability of the failure time. Nevertheless, catastrophic failure occurs in both cases as the correlation length approaches the grain size, which in turn controls the failure of local bridges between aligned en-echelon and wing-cracks in the shear damage zone in the heterogeneous sample. The initial rock microstructure, specifically the anisotropy of pre-existing porosity, dictates the geometry and orientation of the emergent fault plane, independent of starting heterogeneity. This reflects the strong control of starting microstructure on the rock's internal stress state, despite the axisymmetric external loading conditions and the very low anisotropy (1%) inferred from acoustic velocity measurement.

Acknowledgments, Samples, and Data

This work is supported by the UK's Natural Environment Research Council (NERC) through the CATFAIL project NE/R001693/1 'Catastrophic failure: what controls precursory localization in rocks?' We acknowledge the beamline PSICHE at SOLEIL for provision of synchrotron radiation facilities (standard proposal 20160434) and thank our reviewers Jess McBeck and Phil Benson for their thoughtful reviews and suggestions. We would also like to thank the University of Edinburgh Geosciences Workshop for their support in developing the experimental apparatus, and Andy Bell for useful discussions about modelling the correlation length evolution. We declare no conflict of interest. The data supporting our conclusions can be found in main text, the Supporting Information and in the μ CT datasets held at the NERC repository (<http://data.ceda.ac.uk/ngdc/R001693-1>). When using the μ CT datasets, please cite Cartwright-Taylor et al. (2020) and see <https://doi.org/10.5285/0dc00069-8da8-474a-8993-b63ef5c25fb8> for the metadata.

Appendix A. Supporting Information (SI)

Supporting information related to this article can be found in the accompanying document.

References

- Abercrombie, R.E. (1995), Earthquake source scaling relationships from -1 to 5 ML using seismograms recorded at 2.5-km depth, *J. Geophys. Res.* 100, 24015–24036.
- Aki, K. (1965), Maximum likelihood estimate of b in the formula $\log N = a - bM$ and its confidence limits, *Bull. Earthquake Res. Inst.* 43, 237-239.
- Alava, M.J., Nukala, P.K.V. and Zapperi, S. (2008), Fracture size effects from disordered lattice models, *Int. J. Fract.* 154, 51-59.
- Alber, M. and Hauptfleisch, U. (1999), Generation and visualization of micro-fractures in Carrara marble for estimating fracture toughness, fracture shear and fracture normal stiffness, *Int. J. Rock Mech. Min. Sci.* 36, 1065-1071.
- Andrew, M. (2018), A quantified study of segmentation techniques on synthetic geological XRM and FIB-SEM images, *Computational Geosciences* 22, 1503-1512.
- Ashby M.F. and Sammis, C.G. (1990), The damage mechanics of brittle solids in compression, *PAGEOPH* 133, 489-521.
- Ashby, M.F. and Hallam, S.D. (1986), The failure of brittle solids containing small cracks under compressive stress states, *Acta Metall.* 34, 497-510.
- Bandini, A., Berry, P., Bemporad, E., and Sebastiani, M. (2012), Effects of intra-crystalline microcracks on the mechanical behavior of a marble under indentation, *Int. J. Rock Mech. Min. Sci.* 54, 47-55.
- Bell, A.F., Naylor, M. and Main, I.G. (2013a), Convergence of the frequency-size distribution of global earthquakes, *Geophys. Res. Lett.* 40, 2585-2589.
- Bell, A.F., Naylor, M. and Main, I.G. (2013b), The limits of predictability of volcanic eruptions from accelerating rates of earthquakes, *Geophys. J. Int.* 194, 1541-1553.
- Bonnet, E., Bour, O., Odling, N.E., Davy, P., Main, I., Cowie, P. and Berkowitz, B. (2001), Scaling of fracture systems in geological media, *Rev. Geophys.* 39, 347-383.
- Bouchaud, E. (1997), Scaling properties of cracks, *J. Phys. Condens. Matter* 9, 4319-4344.
- Bouchaud, E., Lapasset, G., and Planès, J. (1990), Fractal dimension of fractured surfaces: a universal value?, *Europhys. Lett.* 13, 73-79.
- Brace, W.F., Paulding, B. and Scholz, C. (1966), Dilatancy in the fracture of crystalline rocks. *J. Geophys. Res.* 71, 3939-3953.
- Brantut, N., Baud, P., Heap, M.J. and Meredith, P.G. (2012), Micromechanics of brittle creep in rocks, *J. Geophys. Res.* 117, B08412.
- Brantut, N., Heap, M.J., Baud, P. and Meredith, P.G. (2014), Rate- and strain-dependent brittle deformation of rocks, *J. Geophys. Res. Solid Earth* 119, 1818-1836.
- Bruce, A. and D. Wallace (1989). Critical point phenomena: universal physics at large length scales, in: Davies, P. (ed.), *The New Physics*, Cambridge University Press, Cambridge UK.

- Bruner, W.M. (1984), Crack growth during unroofing of crustal rocks: effects of thermoelastic behavior and near-surface stresses, *J. Geophys. Res.* 89, 4167-4184.
- Bruner, W.M. (1979), Crack growth and the thermoelastic behavior of rocks, *J. Geophys. Res.* 84, 5578-5590.
- Bufe, C.G. and Varnes, D.J. (1993), Predictive modeling of the seismic cycle of the greater San Francisco Bay region, *J. Geophys. Res.* 98, 9871-9883.
- Burnham, K.P. and Anderson, D.R. (2002), *Model selection and multi-model inference: a practical information-theoretic approach* (2nd ed.), Springer, New York.
- Butler, I.B., Flynn, M., Fousseis, F. and Cartwright-Taylor, A. (2017), Mjolnir: a novel x-ray transparent triaxial rock deformation apparatus, ICTMS2017-56, 3rd International Conference on Tomography of Materials and Structures, Lund, Sweden, 26-30 June.
- Cartwright-Taylor, A. (2015), Deformation-induced electric currents in marble under simulated crustal conditions: non-extensivity, superstatistical dynamics and implications for earthquake hazard, PhD thesis, University College London.
- Cartwright-Taylor, A., Main, I.G., Butler, I.B., Fousseis, F., Flynn M. and King, A. (2020): In-situ rock deformation and micron-scale crack network evolution: a high-resolution time-resolved x-ray micro-tomography dataset, British Geological Survey (Dataset) <https://doi.org/10.5285/0dc00069-8da8-474a-8993-b63ef5c25fb8>.
- Ceva, H. and Perazzo, R.P.J. (1993), From self-organized criticality to first-order-like behaviour: A new type of percolative transition, *Phys. Rev. E* 48, 157-160.
- Cho, N., Martin, C.D. and Sego, D.S. (2007), A clumped particle model for rock, *Int. J. Rock Mech. Min. Sci.* 44, 997-1010.
- Clint, O.C., Meredith, P.G. and Main, I.G. (2001), Relation between crack damage and permeability near the percolation threshold in a near perfect crystalline rock, *Geophys. Res. Abstr.* 3, 346.
- Cornelius, R.R. and Voight, B. (1994), Seismological aspects of the 1989-1990 eruption at Redoubt Volcano, Alaska: The Materials Failure Forecast Method (FFM) with RSAM and SSAM seismic data, *J. Volcanol. Geotherm. Res.* 62, 469-498.
- Cowie, P.A., Sornette, D. and Vanneste, C. (1995), Multifractal scaling properties of a growing fault population, *Geophys. J. Int.* 122, 457-469.
- Crawford, B.R., Smart, B.G.D., Main, I.G. and Liakopoulou-Morris, F. (1995). Strength characteristics and shear acoustic anisotropy of rock core subjected to true triaxial compression, *Int. J. Rock Mech. Min. Sci.* 32, 189-200.
- Damjanac, B. and Fairhurst, C. (2010), Evidence for a long-term strength threshold in crystalline rock, *Rock Mech. Rock Eng.* 43, 513-531.
- David, C., Menendez, B. and Darot, M. (1999), Influence of stress-induced and thermal cracking on physical properties and microstructure of La Peyratte granite, *Int. J. Rock Mech. Min. Sci.* 36, 433-448.
- Descoteaux, M., Audette, M., Chinzei, K. and Siddiqi, K. (2005), Bone enhancement filtering: application to sinus bone segmentation and simulation of pituitary surgery, in: Duncan, J.S. and Gerig, G. (eds.), *Proceedings of Medical Image Computing and Computer-Assisted Intervention (MICCAI)*, Palm Springs, California, USA, Lecture Notes in Computer Science 3749, 09-16.

- Desrues, J., Chambon, R., Mokni, M. and Mazerolle, F. (1996), Void ratio evolution inside shear bands in triaxial sand specimens studied by computed tomography, *Geotechnique* 46, 529-546.
- Fairhurst, C. and Cook, N.G.W. (1966), The phenomenon of rock splitting parallel to the direction of maximum compression in the neighborhood of a surface, In: Zeitlen, J.G. (ed) *Proceedings of First Congress of the International Society of Rock Mechanics* (Lisbon, September-October 1966) Vol 1., LNEC, Lisbon, 687-692.
- Faulkner, D.R., Mitchell, T.M., Healy, D. and Heap, M.J. (2006), Slip on 'weak' faults by the rotation of regional stress in the damage zone, *Nature* 444, 922-925.
- Fredrich, J.T., and Wong T.-F. (1986), Micromechanics of thermally induced cracking in three crustal rocks, *J. Geophys. Res.* 91, 12743-12764.
- Fredrich, J.T., Evans, B., and Wong, T.-F. (1989), Micromechanics of the brittle to plastic transition in Carrara marble. *J. Geophys. Res. Solid Earth* 94, 4129-4145.
- Fusseis, F., Steeb, H., Xiao, X., Zhu, W., Butler, I., Elphick, S. and Mäder, U. (2014), A low-cost X-ray-transparent experimental cell for synchrotron-based X-ray microtomography studies under geological reservoir conditions, *J. Synchrotron Rad.* 21, 251-253.
- Girard, L., Amitrano, D. and Weiss, J. (2010), Failure as a critical phenomenon in a progressive damage model, *J. Stat. Mech. Theory Exp.* P01013.
- Goodfellow, S.D. and Young, R.P. (2014), A laboratory acoustic emission experiment under in-situ conditions, *Geophys. Res. Lett.* 41, 3422-3430.
- Graham, C.C., Stanchits, S., Main, I.G. and Dresen, G. (2010), Comparison of polarity and moment tensor inversion methods for source analysis of acoustic emission data, *Int. J. Rock Mech. Min. Sci.* 47, 161-169.
- Greenhough, J. and Main, I.G. (2008), A Poisson model for earthquake frequency uncertainties in seismic hazard analysis, *Geophys. Res. Lett.* 35, L19313.
- Griffith, A.A. (1921), The phenomena of rupture and flow in solids, *Phil. Trans. R. Soc. A* 221, 163-198.
- Griffith, A.A. (1924), Theory of rupture, *Proc. First Int. Congress Appl. Mech.*, Delft, 55-63.
- Griffiths, L., Lengliné, O., Heap, M.J., Baud, P. and Schmittbuhl, J. (2018), Thermal cracking in Westerly granite monitored using direct wave velocity, coda wave interferometry and acoustic emissions, *J. Geophys. Res. Solid Earth* 123, 2246-2261.
- Guéguen, Y. and Schubnel, A. (2003), Elastic wave velocities and permeability of cracked rocks, *Tectonophys.* 370, 163-176.
- Hallbauer, D.K., Wagner, H. and Cook N.G.W. (1973), Some observations concerning the microscopic and mechanical behaviour of quartzite specimens in stiff, triaxial compression tests, *Int. J. Rock Mech. Min. Sci. Geomech. Abstr.* 10, 713-726.
- Haneberg, W.C. (2004), *Computational Geosciences with Mathematica*, Springer-Verlag, Berlin Heidelberg New York.
- Healy, D., Blenkinsop, T.G., Timms, N.E., Meredith, P.G., Mitchell, T.M. and Cooke, M.L. (2015), Polymodal faulting: time for a new angle on shear failure, *J. Struct. Geol.* 80, 57-71.

- Hildebrand, T. and Rügsegger, P. (1997), A new method for the model-independent assessment of thickness in three-dimensional images, *J. Microscopy* 185, 67-75.
- Horii, H. and Nemat-Nasser, S. (1985), Compression-induced microcrack growth in brittle solids: axial splitting and shear failure, *J. Geophys. Res.* 90, 3105-3125.
- Horii, H. and Nemat-Nasser, S. (1986), Brittle failure in compression: splitting, faulting and brittle-ductile transition, *Phil. Trans. R. Soc. A* 319, 337-374.
- Hurvich, C.M. and Tsai, C.-L. (1989), Regression and time series model selection in small samples, *Biometrika* 76, 297-307.
- Kagan, Y.Y. (2002), Seismic moment distribution revisited: i. statistical results, *Geophys. J. Int.* 148, 520-541.
- Kagan, Y.Y. and Schoenberg, F. (2001), Estimation of the upper cutoff parameter for the tapered Pareto distribution, *J. Appl. Probab.* 38, 168-185.
- Kamb, W.B. (1959), Ice petrofabric observations from Blue Glacier, Washington, in relation to theory and experiment, *J. Geophys. Res.* 64, 1891-1909.
- Kandula, N., Cordonnier, B., Boller, E., Weiss, J., Dysthe, D.K. and Renard, F. (2019), Dynamics of microscale precursors during brittle compressive failure in Carrara marble, *J. Geophys. Res. Solid Earth*, 124, 6121-6139.
- Kijko, A. and Graham, G. (1998), Parametric-historic procedure for probabilistic seismic hazard analysis part i: estimation of maximum regional magnitude m_{\max} , *PAGEOPH* 152, 413-442.
- Kilburn, C.R.J. (2003), Multiscale fracturing as a key to forecasting volcanic eruptions, *J. Volcanol. Geotherm. Res.* 125, 271-289.
- Kilburn, C.R.J. and Voight, B. (1998), Slow rock fracture as eruption precursor at Soufriere Hills, *Geophys. Res. Lett.* 25, 3665-3668.
- Kosterlitz, J.M. (1974), The critical properties of the two-dimensional xy model, *J. Phys. C: Solid State Phys.* 7, 1046-1060.
- Kosterlitz, J.M. and Thouless, D.J. (1973), Ordering, metastability and phase transitions in two-dimensional systems, *J. Phys. C: Solid State Phys.* 6, 1181-1203.
- Kranz, R.L. (1979), Crack-crack and crack-pore interactions in stressed granite, *Int. J. Rock Mech. Min. Sci. Geomech. Abstr.* 16, 37-47.
- Kun, F., Pal, G., Varga, I. and Main, I.G. (2018), Effect of disorder on the spatial structure of damage in slowly compressed porous rocks, *Phil. Trans. R. Soc. A* 377, 20170393.
- Kun, F., Varga, I., Lennartz-Sassinek, S. and Main, I.G. (2013), Approach to failure in porous granular materials under compression, *Phys. Rev. E* 88, 062207.
- Lajtai, E.Z. (1974), Brittle fracture in compression. *Int. J. Fract.* 10, 525-536.
- Lei, X. and Satoh, T. (2007), Indicators of critical point behavior prior to rock failure inferred from pre-failure damage, *Tectonophysics*. 431, 97-111.
- Lei, X., Kusunose, K., Nishizawa, O., Cho, A. and Satoh, T. (2000), On the spatiotemporal distribution of acoustic emissions in two granitic rocks under triaxial compression: the role of pre-existing cracks, *Geophys. Res. Lett.* 27, 1997-2000.

- Lennartz-Sassinek, S., Main, I.G., Zaiser, M. and Graham, C.C. (2014), Acceleration and localization of subcritical crack growth in a natural composite material, *Phys. Rev. E* 90, 052401.
- Leonard, T. and Hsu, J.S.J. (1999), *Bayesian Methods*, Cambridge University Press, Cambridge UK.
- Liakopoulou-Morris, F., Main, I.G., Crawford, B.R. and Smart, B.G.D. (1994), Microseismic properties of a homogeneous sandstone during fault nucleation and frictional sliding, *Geophys. J. Int.* 119, 219-230.
- Lockner, D., Byerlee, J.D., Kuksenko, V., Ponomarev, A. and Sidorin, A. (1992), Observations of quasi-static fault growth from acoustic emissions, in: Evans, B. and Wong, T.-F. (eds.), *Fault Mechanics and Transport Properties of Rocks* (1st ed.), *International Geophysics* 51, 3-31.
- Lockner, D., Byerlee, J.D., Kuksenko, V., Ponomarev, A. and Sidorin, A. (1991), Quasi-static fault growth and shear fracture energy in granite. *Nature* 350, 39-42.
- Lomnitz-Adler, J., Knopoff, L. and Martinez-Mekler, G. (1992), Avalanches and epidemic models of fracturing in earthquakes, *Phys. Rev. A* 45, 2211-2221.
- Main, I.G. (1996), Statistical physics, seismogenesis and seismic hazard, *Rev. Geophys.* 34, 433-462.
- Main, I.G., Meredith, P.G., Sammonds, P.R. and Jones, C. (1990), Influence of fractal flaw distributions on rock deformation in the brittle field, in: Knipe, R.J. and Rutter, E.H. (eds.), *Deformation Mechanisms, Rheology and Tectonics*, *Geol. Soc. Spec. Pub.* 54, 81-96.
- Main, I.G. (1992). Damage mechanics with long-range interactions: correlation between the seismic b-value and the two point correlation dimension, *Geophys. J. Int.* 111, 531-541.
- Main, I.G., Sammonds, P.R. and Meredith, P.G. (1993), Application of a modified Griffith criterion to the evolution of fractal damage during compressional rock failure, *Geophys. J. Int.* 115, 367-380.
- Mandelbrot, B., Passoja, D.E., and Paullay, A.J. (1984), Fractal character of fracture surfaces of metals, *Nature* 308, 721-722.
- Meijering, E.H.W. (2010), *FeatureJ 1.6.0*, Biomedical Imaging Group Rotterdam, Erasmus MC, University Medical Center Rotterdam, The Netherlands, 2002-2010 (<http://www.imagescience.org/meijering/software/featurej/>).
- Meredith, P.G., Clint, O.C., Ngwenya, B., Main, I.G., Odling, N.W.A. and Elphick, S.C., (2005), Crack damage and permeability evolution near the percolation threshold in a near-perfect crystalline rock, in: Shaw, R.P., (ed.) *Understanding the Micro to Macro Behavior of Rock-Fluid Systems*, *Geol. Soc. Spec. Pub.* 249, 159-160.
- Meredith, P.G., Main, I.G., Clint, O.C. and Li, L. (2012), On the threshold of flow in a tight natural rock, *Geophys. Res. Lett.* 39, L04307.
- Mignan, A. and Woessner, J. (2012), Estimating the magnitude of completeness for earthquake catalogues. *Community Online Resource for Statistical Seismicity Analysis*, pp. 1-45.
- Mirone, A., Brun, E., Gouillart, E., Tafforeau, P. and Kieffer, J. (2014), The PyHST2 hybrid distributed code for high speed tomographic reconstruction with iterative reconstruction and a priori knowledge capabilities. *Nucl. Instrum. Methods Phys. Res., Sect. B, Beam Interact. Mater. Atoms* 324, 41-48.

- Mitchell, T.M. and Faulkner, D.R. (2012), Towards quantifying the matrix permeability of fault damage zones in low porosity rocks, *Earth Planet. Sci. Lett.* 339-340, 24-31.
- Molli, G. and Heilbronner, R. (1999), Microstructures associated with static and dynamic recrystallization of Carrara marble (Alpi Apuane, NW Tuscany, Italy), *Geologie en Mijnbouw* 78, 119-126.
- Moura, A., Lei, X.-L., Nishizawa, O., 2005. Prediction scheme for the catastrophic failure of highly loaded brittle materials or rocks. *J. Mech. Phys. Solids* 53, 2435–2455
- Nemat-Nasser, S. and Horii, H. (1982), Compression-induced nonplanar crack extension with application to splitting, exfoliation, and rockburst, *J. Geophys. Res.* 87, 6805-6821.
- Nemat-Nasser, S. and Obata, M. (1988), A microcrack model of dilatancy in brittle materials, *J. Appl. Mech.* 55, 24-35.
- Nicksiar, M. and Martin, C.D. (2013), Crack initiation stress in low porosity crystalline and sedimentary rocks, *Eng. Geol.* 154, 64-76.
- Nicksiar, M. and Martin, C.D. (2014), Factors affecting crack initiation in low porosity crystalline rocks, *Rock Mech. Rock Eng.* 47, 1165-1181.
- Nozieres, P. (1992), Shape and growth of crystals, in: Godrèche, C. (ed.), *Solids Far From Equilibrium*, Cambridge University Press, Cambridge UK.
- Odling, N.W.A., Elphick, S.C., Meredith, P., Main, I. and Ngwenya, B.T. (2007), Laboratory measurement of hydrodynamic saline dispersion within a micro-fracture network induced in granite, *Earth Planet. Sci. Lett.* 260, 407-418.
- Oesterling, N. (2004), Dynamic recrystallization and deformation mechanisms of naturally deformed Carrara marble: a study on one- and two-phase carbonate rocks, PhD thesis, University of Basel.
- Ojala I.O., Main, I.G. and Ngwenya, B.T. (2004), Strain rate and temperature dependence of Omori law scaling constants of AE data: implications for earthquake foreshock-aftershock sequences, *Geophys. Res. Lett.* 31, L24617.
- Ollion, J., Cochenec, J., Loll, F., Escudé C. and Boudier, T. (2013), TANGO: A Generic Tool for High-throughput 3D Image Analysis for Studying Nuclear Organization, *Bioinformatics* 29, 1840-1841.
- Olson, J.E., & Pollard, D.D. (1991), The initiation and growth of en échelon veins, *J. Struct. Geol.* 13, 595-608.
- Ouillon, G. and Sornette, D. (2000), The concept of ‘critical earthquakes’ applied to main rockbursts with time-to-failure analysis, *Geophys. J. Int.* 143, 454–468.
- Pál, G., Jánosi, Z., Kun, F. and Main, I.G. (2016). Fragmentation by slow compression of porous rocks, *Physical Review E* 94, 053003.
- Pisarenko, V.F. (1991), Statistical evaluation of maximum possible earthquakes, *Phys. Solid Earth* 27, 757-763.
- Potyondy, D.O. and Cundall, P.A. (2004), A bonded particle model for rock, *Int. J. Rock Mech. Min. Sci.* 41, 1329-1364.
- Ramez, M.R.H. and Murrell, S.A.F. (1964), A petro-fabric analysis of Carrara marble. *Int. J. Rock Mech. Min. Sci. Geomech. Abstr.* 1, 217-229.

- Reches, Z. and Lockner, D.A. (1994), Nucleation and growth of faults in brittle rocks, *J. Geophys. Res.* 99, 18159-18173.
- Renard, F., Cordonnier, B., Dysthe, D.K., Boller, E., Tafforeau, P. and Rack A. (2016), A deformation rig for synchrotron microtomography studies of geomaterials under conditions down to 10 km depth in the Earth, *J. Synchrotron Rad.* 23, 1030-1034.
- Renard, F., Cordonnier, B., Kobchenko, M. and Kandula, N. (2017), Microscale characterization of rupture nucleation unravels precursors to faulting in rocks, *Earth Plan. Sci. Lett.* 476, 69-78.
- Renard, F., Weiss, J., Mathiesen, J. Ben-Zion, Y., Kandula, N. and Cordonnier, B. (2018), Critical evolution of damage toward system-size failure in crystalline rock, *J. Geophys. Res.* 123, 2017JB014964.
- Richter, D. and Simmons G. (1974), Thermal expansion behaviour of igneous rocks, *Int. J. Rock Mech. Min. Sci. Geomech. Abstr.* 15, 145–148.
- Roberts, N.S., Bell, A.F. and Main, I.G. (2015), Are volcanic seismic *b*-values high, and if so when? *J. Volc. Geotherm. Res.* 308, 127-141.
- Robertson, M.C., Sammis, C.G., Sahimi, M. and Martin, A.J. (1995), Fractal analysis of three-dimensional spatial distributions of earthquakes with a percolation interpretation, *J. Geophys. Res.* 100, 609-620.
- Rundle, J.B. and Klein, W. (1989), Nonclassical nucleation and growth of cohesive tensile cracks, *Phys. Rev. Lett.* 63, 171-174.
- Russ, J.C. (1994), *Fractal Surfaces*, Plenum Press, New York.
- Rydelek, P.A. and Sacks, I.S. (1989), Testing the completeness of earthquake catalogues and hypothesis of self-similarity, *Nature* 337, 251–253.
- Sammis, C.G. and Ashby, M.F., (1986), The failure of brittle porous solids under compressive stress states, *Acta Metall.* 34 511-526.
- Sammis, C.G. and Sornette, D. (2002), Positive feedback, memory and the predictability of earthquakes, *PNAS* 99, 2501-2508.
- Sammonds, P.R., Meredith, P.G. and Main, I.G. (1992), Role of pore fluids in the generation of seismic precursors to shear fracture, *Nature* 359, 228-230.
- Schindelin, J., Arganda-Carreras, I., Frise, E., Kaynig, V., Longair, M., Pietzsch, T., Preibisch, S., Rueden, C., Saalfeld, S., Schmid, B., Tinevez, J.Y., White, D.J., Hartenstein, V., Eliceiri, K., Tomancak, P., Cardona, A., (2012), Fiji: an open-source platform for biological-image analysis, *Nature Methods* 9, 676–682.
- Schmittbuhl, J. and Maloy, K.J. (1997), Direct observation of a self-affine crack propagation, *Phys. Rev. Lett.* 78, 3888-3891.
- Schmittbuhl, J., Schmitt, F., and Scholz, C. (1995), Scaling invariance of crack surfaces, *J. Geophys. Res.* 100, 5953-5973.
- Sethna, J.P. (2006). *Statistical mechanics: entropy, order parameters, and complexity*. Oxford University Press, Oxford UK.
- Simmons, G. and Cooper, H.W. (1978), Thermal cycling cracking in three igneous rocks, *Int. J. Rock Mech. Min. Sci. Geomech. Abstr.* 15, 145-148.

- Smith, R., Sammonds, P.R. and Kilburn, C.R.J. (2009), Fracturing of volcanic systems: experimental insights into pre-eruptive conditions, *Earth Planet. Sci. Lett.* 280, 211-219.
- Sornette, D. (2006), *Critical phenomena in natural sciences: chaos, fractals, self-organization and disorder: concepts and tools*, Springer, Berlin.
- Sornette, D. (2009), Dragon-kings, black swans and the prediction of crises, in press in the *Int. J. of Terraspace Sci. and Eng.* 2, 1-18, <https://arxiv.org/abs/0907.4290>
- Sornette, D. and Sammis, C.G. (1995), Complex critical exponents from renormalization group theory of earthquakes: implications for earthquake predictions, *J. Phys. I [French]* 5, 607-619.
- Stanley, H.G. (1971), *Introduction to phase transitions and critical phenomena*, Oxford University Press, Oxford UK.
- Sykes, L.R. and Jaumé, S. (1990), Seismic activity on neighboring faults as a long-term precursor to large earthquakes in the San Francisco Bay area, *Nature* 348, 595–599.
- Tapponnier, P. and Brace, W.F. (1976), Development of stress-induced microcracks in Westerly granite, *Int. J. Rock Mech. Min. Sci. Geomech. Abstr.* 13, 103-112.
- Thomas, A.L., & Pollard, D.D. (1993), The geometry of echelon fractures in rock: implications from laboratory and numerical experiments, *J. Struct. Geol.* 15, 323-334.
- Thouless (1989), *Condensed matter physics in less than three dimensions*, in: Davies, P. (ed.), *The New Physics*, Cambridge University Press, Cambridge UK.
- Turcotte, D. (1997), *Fractals and chaos in geology and geophysics*, Cambridge University Press, Cambridge UK.
- Tyupkin, Y.S. and Giovambattista, R.D. (2005), Correlation length as an indicator of critical point behavior prior to a large earthquake, *Earth Planet. Sci. Lett.* 230, 85–96.
- Utsu, T., Ogata, Y. and Matsu'ura, R.S. (1995), The centenary of the Omori formula for a decay law of aftershock activity, *J. Phys. Earth* 43, 1-33.
- Vasseur, J., Wadsworth, F.B., Heap, M.J., Main, I.G., Lavallée, Y. and Dingwell, D. B. (2017), Does an inter-flaw length control the accuracy of rupture forecasting in geological materials? *Earth Plan. Sci. Lett.* 475, 181-189.
- Vasseur, J., Wadsworth, F.B., Lavallée, Y., Bell, A.F., Main, I.G. and Dingwell, D. B. (2015), Heterogeneity: the key to failure forecasting, *Sci. Rep.* 5, 13259.
- Vinciguerra, S., Trovato, C., Meredith, P.G. and Benson P.M. (2005), Relating seismic velocities, thermal cracking and permeability in Mt. Etna and Iceland basalts, *Int. J. Rock Mech. Min. Sci.* 42, 900–910.
- Voight, B. (1988), A method for prediction of volcanic eruptions, *Nature* 332, 125-130.
- Voorn, M., Exner, U. and Rath, A. (2013), Multiscale Hessian fracture filtering for the enhancement and segmentation of narrow fractures in 3D image data, *Comp. Geosci.* 57, 44-53.
- Weiss, J. (2001), Self-affinity of fracture surfaces and implications on a possible size effect on fracture energy, *Int. J. Fract.* 109, 365-381.

Accepted Article

Woessner, J. and Wiemer, S. (2005), Assessing the quality of earthquake catalogues: estimating the magnitude of completeness and its uncertainty, *Bull. Seismol. Soc. Am.* 95, 684-698.

Zhang, S., Cox, S.F., and Paterson, M.S. (1994), The influence of room temperature deformation on porosity and permeability in calcite aggregates. *J. Geophys. Res. Solid Earth*, 99, 15761-15775.

Zöller, G., Hainzl, S. and Kurths, J. (2001), Observation of growing correlation length as an indicator for critical point behavior prior to large earthquakes, *J. Geophys. Res.* 106, 2167-2175.